Chinese Chemical Letters 34 (2023) 107527

Contents lists available at ScienceDirect

Chinese Chemical Letters

journal homepage: www.elsevier.com/locate/cclet

Applications of metal nanoparticles/metal-organic frameworks composites in sensing field

Jinming Xu, Jiao Ma, Yi Peng, Shuai Cao, Songtao Zhang, Huan Pang*

School of Chemistry and Chemical Engineering, Yangzhou University, Yangzhou 225009, China

ARTICLE INFO

Article history:
Received 2 April 2022
Revised 25 April 2022
Accepted 12 May 2022
Available online 16 May 2022

Keywords:
Metal nanoparticles
Metal-organic frameworks
Composites
Sensing application
Synergistic effects

ABSTRACT

Metal nanoparticles (MNPs) possess size-dependent desirable electronic and optical properties while metal-organic frameworks (MOFs) have an edge over extremely large specific surface areas, homogeneous structure, high porosity and remarkable chemical stability. Their combination (MNPs/MOFs) is a novel nanomaterial with broad application prospect in sensing field. To improve performance in sensing applications, we have paid great attention to synergistic effects between the two compositions above. Because of the synergistic effects between MNPs and MOFs, sensors on the basis of MNPs/MOFs composites show significant sensing enhancement with respect to stability, selectivity and sensitivity. In this review, various applications for MNPs/MOFs composites in electrochemical sensing, fluorescent sensing, colorimetric sensing, surface-enhanced Raman scattering sensing and chemiluminescence/electrochemiluminescence sensing are focused and summarized. Besides, the synergistic interactions between MNPs and MOFs was investigated. Finally, based on theoretical information from the reports as well as experimental experience, this review offers the challenges and opportunities for future research on MNPs/MOFs composites.

1. Introduction

In the past few decades, important advances in colloid and surface chemistry have given rise to large quantities of fundamental and applied studies in nano precious metals. For example, metal nanoparticles (MNPs) serve as a hot spot currently by researchers [1,2]. MNPs possess size-dependent physicochemical characteristics, which not only enables them to be applied to sensitive sensing in bioanalysis, but also helps them to detect varieties of biological processes *via* color shift, fluorescence adjustment and spectrum intensification [3–8]. The aforementioned MNP-based expanded applications, are readily functionalized by recognition elements such as deoxyribonucleic acid, protein and antibody, providing perfect selectivity to various biological objectives [9–14]. In particular, taking advantage of their satisfying optical and electronic characteristics [15,16], MNPs have been widely applied in sensing in the last several years. Typically, both gold nanoparticles and silver nanoparticles are popular in electrochemical sensors [17–19]. Localized surface plasmon resonance (LSPR) is a phenomenon occurring at certain light frequencies [20]. Because external electromagnetic radiation interferes with collective electron oscillations in the conduction band, MNPs have distinctive electronic and optical properties consequently [21]. The electron cloud is pushed away from its equilibrium state by this electromagnetic force, which causes polarization of the surface. Then oscillatory motion fosters and the balance of system recovers. The LSPR bands of gold (Au), silver (Ag) and copper (Cu) are located in the visible region, while the plasmon bands of transition metals are located in the UV region, enabling them attractive optical candidates [22]. Whereas, as Cu can be easily oxidized [23], most work associated with MNP has been immersed in Au and Ag. Metal nanoparticles tend to migrate and coalesce at high reaction temperatures due to their high surface energy and thermodynamic instability. Structure changes are ordinarily accompanied by sharp declines when it comes to selectivity and catalytic activity. Therefore, if metal nanoparticles are encapsulated in nanoshells or nanopores and immobilized on support structures, they are unable to get access to metal nanoparticles, stop aggregating and migrating, and improve catalytic stability [24–29]. Metal-organic frameworks (MOFs) are a novel type of porous materials composed of metal ions or clusters and organic linkers [30–39], which serves as a promising candidate material for MNP carrier. MOFs possess super-large surface area, orderly configuration, multi-functionality pore sizes, remarkable chemical stability and high bioaffinity to biomolecules [40–42]. Thus, MOFs can accommodate massive numbers of MNPs effectively, preventing migration while enhancing their stability [43–49]. MNPs/MOFs composites, which are multifunctional MNPs en-

* Corresponding author.
E-mail address: panghuan@yzu.edu.cn (H. Pang).

https://doi.org/10.1016/j.cclet.2022.05.041
1001-8417/

cased in MOFs either on MOFs, have achieved excellent sensing performance on account of synergistic effect and been widely used in diverse sensing areas.

The synergistic effects between MNPs and MOFs are replete with diversity and complexity, according to the sensing application of MNPs/MOFs composites. The synergistic effects of the composites employed in sensing tends to be attributed to four general synergistic mechanisms [44,48]. (1) MNPs function as active sites while MOFs play a significant role in immobilizing and stabilizing MNPs, endowing their composites with superior catalytic performance, which are extensively employed in electrochemical, colorimetric and SERS sensors. (2) MOFs effectively confine aggregated MNPs and improve the detectable signal generally in fluorescent sensors. Some typical metal nanoclusters (MNCs), involving Au and Ag nanoclusters, perform excellent fluorescence characteristics at the expense of low quantum yields [50,51]; in this case, MOFs may be applied to retain these MNCs in their aggregated conditions by confining their free mobility, thus improving quantum yields and aggregation-induced emission [52,53]. (3) MOFs command size selectivity on account of their porous nature, whereas MNPs function as active centers. When it comes to core-shell structural MNPs/MOFs composites, the MOFs allows target molecules with smaller pores than MOFs to enter the internal MNPs, whereas macromolecules are denied access [54–56]. Since MOFs act as a molecular sieve, sensors established on such structure of composites show better selectivity and satisfying anti-interference performance. (4) Either MNPs or MOFs function as active centers in tandem catalytic reactions. The design of such composites is to apply MNPs and MOFs as the active sites to synergistically catalyze the cascade reaction, especially in colorimetric sensors and chemiluminescence/electrochemiluminescence sensors [57]. The MNPs/MOFs composites benefit from the special synergistic mechanism above, which enables the sensing system with more effectivity, sensitivity and selectivity than the conventional sensing systems.

Though large quantities of sensors based on MNPs/MOFs composites have been reported so far, researches on MNPs/MOFs are still in early stages since most reports are concentrated on the stabilization of MNPs by MOFs and debate on the excellent properties of MNPs [58]. In this review, we summed up the extensive applications of MNPs/MOFs composites in sensing field and definitely indicate that the synergistic effect between MNPs and MOFs efficiently integrates their several numerous edges, leading to an improved sensing performance. We offered a review of MNPs/MOFs composites as to sensing application (Fig. 1). To complete this review, we summarized numerous kinds of MNPs/MOFs composites based on sensors and demonstrate certain significant concerns. Most importantly of all, synergistic effects are underlined between the two compositions in MNPs/MOFs as to improved sensing performance. It is hoped that our overview will provoke the interests and passions of scientists in chemistry and biology and will encourage them to have a more comprehensive understanding of the research on MNPs/MOFs composites, thus developing further exploitation and advances of relevant research areas.

2. Applications of MNPs/MOFs composites in sensing

2.1. Electrochemical sensors

Electrochemical sensors can transform chemical signals into electrical signals. Due to their unique properties, there are great possibilities that MNPs/MOFs composites have potential applications in electrochemical sensors and can play various roles in electrochemical biosensing. More specifically, MNPs/MOFs composites own an edge over high porosity, large surface areas and strong bio-affinity, and may be used as support platforms for biological molecules immobilization. Meanwhile, related reactions can be catalyzed by MNPs/MOFs composites to generate efficient electrochemical signals which are detectable because of their distinctive catalytic activity, outstanding stability, and splendid conductivity. Here, the reported MNPs/MOFs composites which are used to prepare electrochemical sensors are categorized on the basis of the functions of MNPs/MOFs composites (Table 1).

2.1.1. Support platforms

Since biological molecules must be immobilized on the sensor interface for electrochemical sensing to operate, which is an important stage in the sensor preparation process. The sensitivity and precision of the sensor is determined by the number and stability of immobilized biomolecules. MNPs/MOFs composites have a broad application prospect as s support platform for biomolecular immobilization. The porous and chemically stable MOFs offer quantities of load sites and protective microenvironments to MNPs, which appeal to biomolecules through electrostatic adsorption. Therefore, immobilized MNPs/MOFs composites may be employed to support various biomolecules desired as for electrochemical sensing applications.

With regard to electrochemical immunosensors, MNPs/MOFs composites are identified as viable and available support platforms to motivate antigen-antibody reactions [59–63]. For instance, Dong *et al.* proposed an enzyme-free electrochemical immunosensor to detect calprotectin (CALP) featuring PtNi@Cu-TCPP(Fe) (TCPP(Fe) = Fe(III) *meso*-tetra(4-carboxyphenyl) porphine chloride) hybrid nanosheets to constitute support platform (Fig. 2A) [59]. In order to maximize the surface area of antibody immobilization and provide a specific active site for antibody (Ab_2) detection, PtNi nanospheres were loaded onto the Cu-TCPP(Fe) surface. When detecting target CALP, the prepared Ab_2/PtNi@Cu-TCPP(Fe) were constructed on the surface of modified electrode on the basis of the sandwich immunological response. According to the above procedures, the limit of detection (LOD) of the synthesized sandwich CALP immunosensor was 0.1377 ng/mL, with a linear response range of 0.2-50 ng/mL. Similarly, Zhao *et al.* synthesized Au/Co-BDC/MoS_2 with the two-dimensional metal-organic framework (Co-BDC) hybridized with MoS_2 nanosheets to load gold nanoparticles (Fig. 2B) [60]. The synthesized Au/Co-BDC/MoS_2 performed relatively low catalytic activity and perfect electrical conductivity instead, which was applied to load primary antibodies to effectively boost the sensitivity. After the capture of target dendritic platinum-copper alloy nanoparticles, the signal amplification tags, MoS_2-labeled secondary antibodies, were brought in to obtain a sandwich-type electrochemical immunosensor achieving a linearity response range of 10 fg/mL–100 ng/mL with the LOD of 3.02 fg/mL. Au nanoparticle-implanted zinc-based metal-organic frameworks (Au@MOFs) were uiltilized as substrates by Ma *et al.* to modify the electrodes and immobilize the primary antibodies (Fig. 2C) [61]. By covalent bonding, free amino groups on Au@MOF surface might efficiently boost the quantity of primary antibodies immobilization. Concurrently, the conductivity of MOFs was enhanced due to the embedding of Au NPs, with interface electron shift accelerating. Second antibodies were labeled using sub-30 nm Au@Pd^Pt nanocubes placed on ultrathin MnO_2 nanosheets. Because of significant antibodies loading on the Au@Pd^Pt NCs platform, a wide linear range (10 fg/mL–100 ng/mL) was accomplished, as well as a low LOD of 4.17 fg/mL.

Other biological recognition components, including nucleic acid [64] and aptamers [65,66] have been discovered to be immobilized by MNPs/MOFs composites as well. Zhang *et al.* constructed cerium dioxide-functionalized carboxyl fullerene (c-C_{60}), which was supported by Pt NPs (c-C_{60}/CeO_2/PtNPs) to amplify signal (Fig. 2D) [64]. Meanwhile, they manufactured AuNPs@Fe-MOFs as a support platform and used a one-step technique to strengthen the

Table 1
Electrochemical sensors based on MNPs/MOFs composites.

Nanomaterial	Analyte	Linear response range	Detection limit	Ref.
Support platforms				
PtNi@Cu-TCPP(Fe)	Calprotectin	200 fg/mL–50 ng/mL	137.7 fg/mL	[59]
Au/Co-BDC/MoS_2	Cardiac troponin I	10 fg/mL–100 ng/mL	3.02 fg/mL	[60]
Au@MOFs	Neuron-specific enolase	10 fg/mL–100 ng/mL	4.17 fg/mL	[61]
Au NPs@ZIF-8	Carcinoembryonic antigen	5 pg/mL–400 ng/mL	1.3 pg/mL	[62]
Au NPs@MIL-101	Anti microcystin-LR	0.05 ng/mL–75 mg/mL	0.02 ng/mL	[63]
Au@Fe-MIL-88	CYP2C19*2	1 fmol/L–50 nmol/L	0.33 fmol/L	[64]
Ti-MOF-Pt	Thrombin	4 pmol/L–0.2 μmol/L	1.3 pmol/L	[65]
AuNPs/Fc-KB/ZIF-8	Vanillin	10 nmol/L–0.2 mmol/L	3 nmol/L	[66]
Catalysts				
AuNPs/Co-MOF/MWCNT	Nitrite	1–1000 μmol/L	0.4 μmol/L	[67]
Au@UiO-66(NH_2)	Hepatitis viral antigens	1.13 fg/mL–100 ng/mL	1.13 fg/mL	[68]
Cu-MOF/Au	Nitrite	0.1 μmol/L–4 mmol/L; 4-10 mmol/L	82 nmol/L	[69]
GOx@ZIF-8(AuNPs)	Glucose	0.05–0.45 μmol/L	50 nmol/L	[70]
Au/ZIF-L	Acetaminophen	0.056–0.56 mmol/L	1.02 μmol/L	[71]
Au/NH_2-UiO-66	Streptomycin	0.005–150 ng/mL	2.6 pg/mL	[72]
Pt@UiO-66-2	Hydrazine	0–1000 μmol/L 1000–4000 μmol/L	0.024 μmol/L	[73]
Pt@UiO66-NH_2	Malathion	1×10^{-14} –1×10^{-9} mol/L	4.9×10^{-15} mol/L	[74]
Pt/Fe-MIL-88	FGFR3 mutation gene	0.1 fmol/L–1 nmol/L	0.033 fmol/L	[75]
Pt-UiO-66	Phosalone	0.50 nmol/L–20 μmol/L	0.078 nmol/L	[76]
Pt@UiO-66-NH_2	Telomerase	5×10^2–10^7 HeLa cell/mL	100 HeLa cell/mL	[77]
Pt@MIL-101(Cr)	Xanthine	0.5–162 mmol/L	0.42 mmol/L	[78]
Pt@Cu-MOF	Carcinoembryonic antigen	–	0.023 pg/mL	[79]
Ag/ZIF-8	Hydrazine	6–5000 μmol/L	0.08 μmol/L	[80]
Ag@Zn-TSA	Hydrogen peroxide	0.3–20,000 μmol/L	0.08 μmol/L	[81]
	Glucose	2.0–1022 μmol/L	0.8 μmol/L	
	Nitrite	1.3–1660 μmol/L 2262–133,000 μmol/L	0.5 μmol/L	
AgNPs/MIL-101	Tryptophan	1–50 μmol/L; 50–150 μmol/L	0.14 μmol/L	[82]
Ag/Zn-MOF	H_2O_2	1 μmol/L–5 mmol/L	67 nmol/L	[83]
Ag/Fe-MOF	α2,6-Sial-Gs	1 fg/mL–1 ng/mL	0.09 fg/mL	[84]
$Cu_3(BTC)_2$-Ag	Diethylstilbestrol	0.005–500 ng/mL	1.67 pg/mL	[85]
Ag@MOF	Cu(II)	1–50 mol/L	0.68 μmol/L	[86]
	Pb(II)	1–50 μmol/L	0.64 μmol/L	
AgNPs/PCN-224	Telomerase	1.0×10^{-7}–1.0×10^{-1} IU/L	5.4×10^{-8} IU/L	[87]
Pd/NH_2−MIL-101(Cr)	Nitrite	5–150 nmol/L	1.3 nmol/L	[88]
Pd/NH_2−MIL-101	Telomerase	5×10^2–1.62×10^7 cells/mL	11.25 cells/mL	[89]
Pd/UiO-66	Microrna-21	20 fmol/L–600 pmol/L	0.713 fmol/L	[90]
Cu@ZIF-8	Glucose	5 μmol/L–3 mmol/L	1.97 μmol/L	[91]
Cu/ZIF-8	Glucose	–	2.76 μmol/L	[92]
Ni/NiO/Ni-MOF	Glucose	4–5664 μmol/L	0.8 μmol/L	[93]
Co-MOFs/PtPdNPs	Thrombin	1 pmol/L–30 nmol/L	0.32 pmol/L	[94]
PdPt/Fe-MOF	Pb^{2+}	0.005–1000 nmol/L	2 pmol/L	[95]
AuPd@MIL-88	Pb^{2+}	5.0 pmol/L–2.0 μmol/L	0.07 pmol/L	[96]
AuPd/NH_2-UiO-66	Nitrite	0.05–5666 μmol/L	0.01 μmol/L	[97]
AuPd@UiO-67	Hg^{2+}	1.0 nmol/L–1.0 mmol/L	0.16 nmol/L	[98]
AgPd@UiO-66-NH_2	4-Nitrophenol	100–370 μmol/L	32 nmol/L	[99]
AgPt/PCN-223-Fe	Ochratoxin A	20 fg/mL–2 ng/mL	14 fg/mL	[100]
AuCu/PPy/Cu-TCPP	H_2O_2	7.10 μmol/L–24.10 mmol/L	6.67 nmol/L	[101]
CuAu/Co-MOFs	NMP-22	0.1 pg/mL–1 ng/mL	33 fg/mL	[102]
MOF-Au@Pt	H_2O_2	0.8 μmol/L–3 mmol/L	86 nmol/L	[103]
NiPd@Ni_3HHTP_2	H_2O_2	1.0 μmol/L–45.0 mmol/L	0.8 μmol/L	[104]
Ag@ZIF-67	Glucose	2–1000 μmol/L	0.66 μmol/L	[105]
Pd/NH_2-ZIF-67	Prostate-specific antigen	100 fg/mL–50 ng/mL	0.03 pg/mL	[106]
Ag@ZIF-67	Hydrogen peroxide	5.0–275 μmol/L 775–2775 μmol/L 4775–16775 μmol/L	1.5 μmol/L	[107]
Ag/H-ZIF-67	Hydrogen peroxide	5 μmol/L–7 mmol/L; 7–67 mmol/L	1.1 μmol/L	[108]
Pt@Co(II)MOF	Thrombin	0.1 pmol/L–50 nmol/L	0.33 fmol/L	[109]
Au@NH_2−MIL-125(Ti)	Bovine serum albumin	10^{-18}–10^{-12} g/mL	4.147×10^{-19} g/mL	[110]
Cu_3P@NH_2−MIL-125(Ti)	Hydrazine	5 μmol/L–7.5 mmol/L	79 nmol/L	[111]
Au/Ag-MOF	Carcinoembryonic antigen	0.05–120 ng/mL	8.0 fg/mL	[112]
Au@Cu_2O-MIL-53(Fe)	H_2O_2	10–1520 μmol/L	1.01 μmol/L	[113]
Cu-MOFs/Au	Hg^{2+}	10 fmol/L–100 nmol/L	4.8 fmol/L	[114]
pSC_4-AuNPs/Cu-MOFs	Fractalkine	–	7.4 pg/mL	[115]
Pd/PCN-224	DNA	100 fmol/L–100 nmol/L	33.6 fmol/L	[116]
Au-SO_3_NU-902	Nitrite	0–2.0 mmol/L	9.1 μmol/L	[117]
AuNPs/MMPF-6(Fe)	Hydroxylamine	0.01–1.0 μmol/L; 1.0–20.0 μmol/L	0.004 μmol/L	[118]
Au NPs/UiO-66	H_2O_2	0.2–23 mmol/L	0.045 μmol/L	[119]
PtCu@MOF-74	H_2O_2	–	0.23 μmol/L	[120]
PtCu@HKUST-1		–	0.22 μmol/L	
Cu_xO@ZIF-8	H_2O_2	1.5–21,442 μmol/L	0.15 μmol/L	[121]
Ag@Y-1,4-NDC-MOF	H_2O_2	4–11,000 μmol/L	0.18 μmol/L	[122]
Cu@Y-1,4-NDC-MOF		4–8500 μmol/L	0.43 μmol/L	

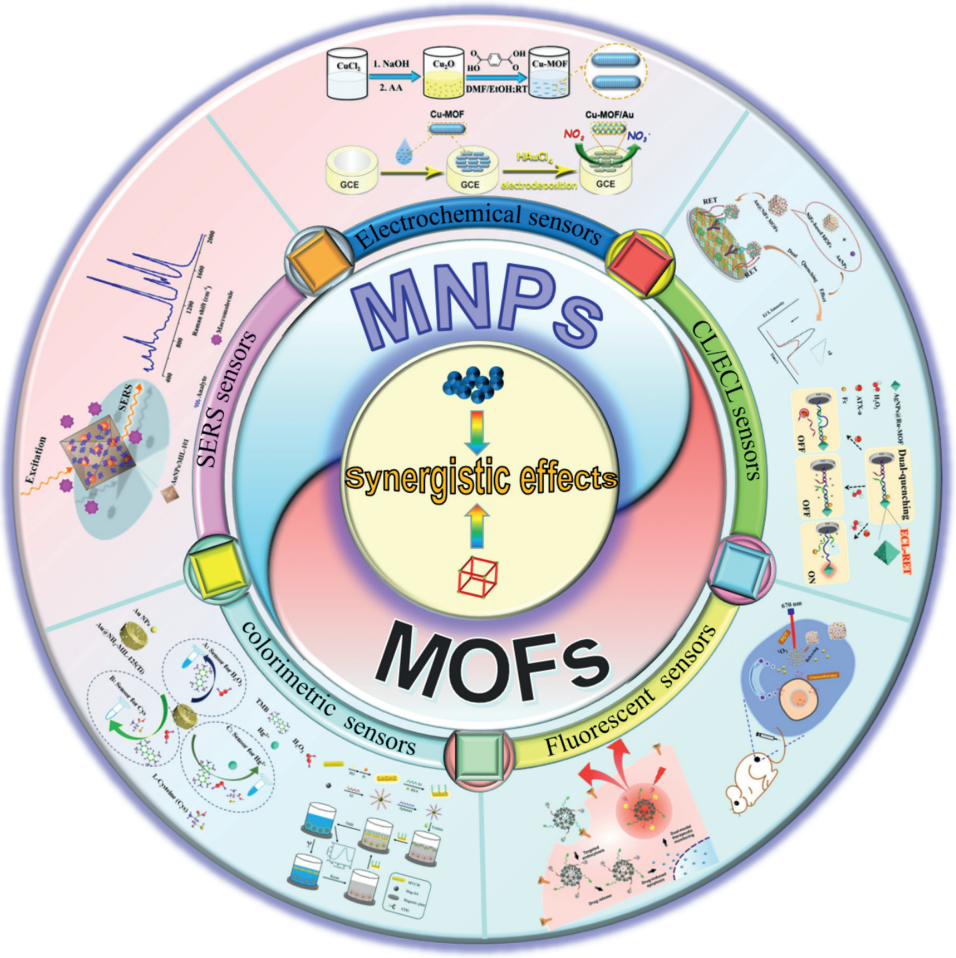

Fig. 1. Sensors based on MNPs/MOFs composites and their applications.

conductivity of streptavidin and biotin through affinity and specificity, and additional biotin-modified capture probes were immobilized. The signal tag was constituted of c-C_{60}/CeO_2/PtNPs that had been tagged with signal probe. After the sandwich response of CYP2C19*2 gene within capture probe and signal tag, an electrochemical signal of CYP2C19*2 gene was observed through the signal tag. Electrochemical signal was recorded by amperometry. Under optimized conditions, an excellent linear dependency was established: current and logarithm of CYP2C19*2 gene concentrations ranging from 1 fmol/L to 50 nmol/L with a LOD of 0.33 fmol/L. An aptasensor employing a Ti-MOF-Pt as support platform was developed by Jiang *et al.* to achieve thrombin detecting [65]. They used firm interaction among the four pyrrole nitrogen atoms in the porphyrin rigid skeleton to fix monoatomic Pt in Pt^{II} tetrakis(4-carboxyphenyl)porphyrin (PtTCPP). To speed up charge transmission, Ti-oxo clusters were employed as metal nodes as well. It indicated that by inserting monoatomic platinum into the middle of a two-dimensional porphyrin framework, the electrochemical performance of MOF could be improved, with a detection limit of 1.3 pmol/L for thrombin and high sensitivity following aptamer immobilization. Sun *et al.* proposed a simple and ultrasensitive ratiometric electrochemical sensor detecting vanillin, which was on the basis of dual-mingled ketjen black (KB) and ferrocene (Fc) MOF on glassy carbon electrodes (GCE) and then *in-situ* electrodeposition of gold nanoparticles coupled with DNA aptamer (Fig. 2E) [66]. Subsequently, the aptamer-AuNPs/Fc-KB/ZIF-8@GCE sensing platform was obtained by coupling AuNPs with a 5′-SH ended aptamer of vanillin through Au-S bonding. Vanillin was bound to its aptamer on gold nanoparticles specifically, resulting in coiled and binding vanillin-aptamer complexes on AuNPs/Fc-KB/ZIF-8@GCE. Vanillin performed a routinely enhanced peak current intensity (I_{van}) during conjunction due to its tendency to get access to the surface of electrode. There were inappreciable changes of Fc doped into ZIF-8 in its peak current intensity (I_{Fc}). In the region of 10 nmol/L to 0.2 mmol/L, the logarithm of I_{van}/I_{Fc} and vanillin concentration demonstrated a strong linear relationship, accompanied by a LOD of 3 nmol/L.

2.1.2. Catalysts

MNPs function as active sites and MOFs act as the protective carrier. MOFs with high porosity have revealed to be desired carriers for MNPs because of their adjustable pore environment. MNPs show better stability and enhanced catalytic activity after loading on MOFs. As to MNPs/MOFs composites, MNPs function as the active sites, which are protected by MOFs, preventing its aggregation and maintaining its catalytic performance. The discussed above supposes to be the most frequent congenerous effect for MNPs/MOFs composites as electrochemical sensor catalysts.

Varieties of MNPs exhibiting excellent electrocatalytic activity, including Au NPs [67–72], Pt NPs [73–79], Ag NPs [80–87], Pd NPs [88–90], Cu NPs [91,92], Ni NPs [93] and various bimetallic NPs [94–104], are appropriate to encapsulate in or on MOF, working as catalysts as for electrochemical sensing.

In accordance with foregoing reports, Au/MOFs have been extensively employed as electrocatalysts in electrochemical sensing

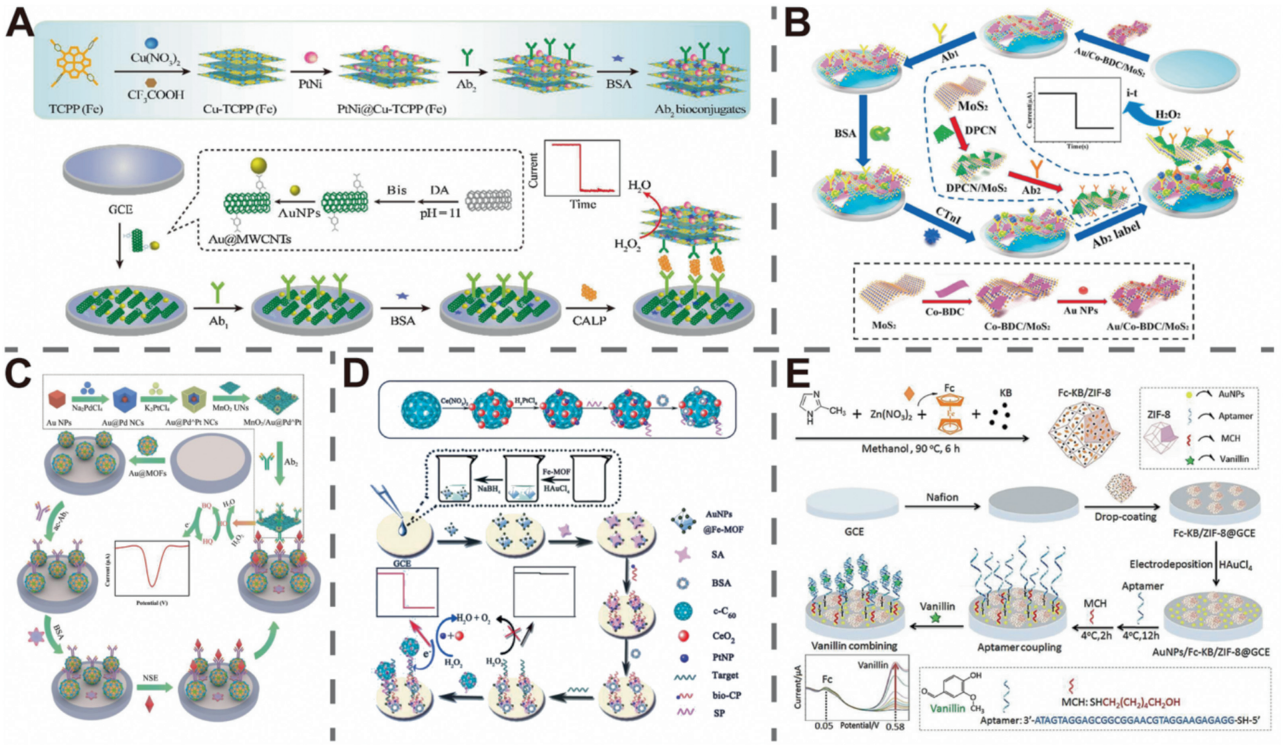

Fig. 2. (A) The preparation procedure of PtNi@Cu-TCPP(Fe)-Ab_2 bioconjugates and schematic illustration of the construction process of the sandwich electrochemical immunosensor. Reproduced with permission [59]. Copyright 2020, Elsevier. (B) Schematic illustration of the preparation of Au/Co-BDC/MoS_2 immunosensor. Reproduced with permission [60]. Copyright 2021, Elsevier. (C) Schematic illustration of the preparation process of MnO_2 UNs/Au@Pd^Pt NCs-Ab_2 and fabrication procedure of the immunosensor. Reproduced with permission [61]. Copyright 2020, American Chemical Society. (D) The preparation process of the c-C_{60}/CeO_2/PtNPs/SP signal probes and schematic illustration of the assembly procedure of the electrochemical biosensor. Reproduced with permission [64]. Copyright 2018, Elsevier. (E) Schematic illustration of the fabrication of a proposed aptasensor based on AuNPs/Fc-KB/ZIF-8 for detecting vanillin. Reproduced with permission [66]. Copyright 2019, Elsevier.

because of their prominent electrocatalytic activity and electrical conductivity. To our knowledge, in the field of electrochemical sensing, there have been large quantities reports about Au/MOFs detection of different analytes [67–72]. For instance, a layered structure based on multiwalled carbon nanotube (MWCNT), Co-based MOF and highly distributed small Au nanoparticles was proposed by Lei *et al.* [67]. Small Co-MOF nanoplates were firstly loaded on the surface of the conductive MWCNT, and then acted as polyporous carrier to provide plentiful adsorption sites for capturing Au ions. The Co-MOF was considerable in adjusting the dispersion of AuNPs, and restricting particle growth during reduction. Electron transfer capability of Co-MOF could extremely be enhanced by integrating MWCNT with Co-MOF. Additionally, AuNPs with small size and high uniformity dispersed on Co-MOF could pull down the operating voltage and observably enhance their catalytic activity to oxidate nitrite. Since the intriguing synergy between the constituents, the prepared AuNPs/Co-MOF/MWCNT sensor performed a linear response ranging from 1 μmol/L to 1000 μmol/L with a LOD of 0.4 μmol/L at a low operating voltage of 0.72 V. By employing an immunofunctionalized zirconium-based MOF, Bajpai *et al.* fabricated a sensitive electrochemical biosensor which could allowed the fabrication of large-surface-area MOF featuring splendid stability with Au modification Au@UiO-66(NH_2) composite-coated GCE to determine infectious hepatitis B surface antigen (HBsAg) (Fig. 3A) [68]. Through immunofunctionalization, Au nanoparticles were embedded into UiO-66(NH_2), and GCE was prepared by anti-HBsAg immunofunctionalization to enhance its catalytic performance. The electrochemical sensing capability of the immunofunctionalized Au@UiO-66(NH_2)/GCE with HBsAg was characterized using cyclic voltammetry and differential pulse voltammetry. The results revealed a linear dynamic connection between the electrical signal and HBsAg levels ranging from 1.13 fg/mL to 100 ng/mL with a LOD of 1.13 fg/mL under optimized settings.

Similar to Au NPs, Pt NPs perform superior catalytic performance for varieties of analyte reactions as well. Therefore, Pt/MOFs composites have been extensively employed in the progress of electrochemical sensing [73–79]. Ma *et al.* successfully synthesized Pt@UiO66-NH_2 featuring large surface area and well-dispersed Pt NPs, and employed it to obtain acetylcholinesterase sensors to detect organophosphorus pesticides in quick succession [74]. The pores of UiO66-NH_2 could adequately disperse Pt NPs and promote mass conveyance and prevent Pt NPs from migrating and aggregating. The developed biosensor showed not only good sensitivity to malathion due to excellent electron conduction channels but also an increase in Pt@UiO66-NH_2 adsorption sites, and high specific surface area for increased acetylcholinesterase immobilization as well. Malathion detected showed perfect linearity ranging from 0.01 mol/L to 1 nmol/L and 4.9×10^{-15} mol/L was considered as LOD. Xu *et al.* successfully synthesized a Pt-doped UiO-66 decorated carbon paste microelectrode (CPME) featuring ordered heterojunctions with excellent electrocatalytic activity (Fig. 3B) [76]. Pt-UiO-66 featuring isolated distributed Pt NPs active sites was added to the CPME, which offered a considerably increased signal for voltammetry. Electropolymerization and a sol-gel technique were subsequently used to create a mesoporous molecularly imprinted polymer on Pt-UiO-66/CPME that could incorporate the phosalone template molecules through multiple bonds. Consequently, the obtained sensor had a good linearity of concentration in the range of 0.50 nmol/L–20 μmol/L, with a LOD of 0.078 nmol/L, performing outstanding repeatability, reproducibility, and stability to analyze phosalone.

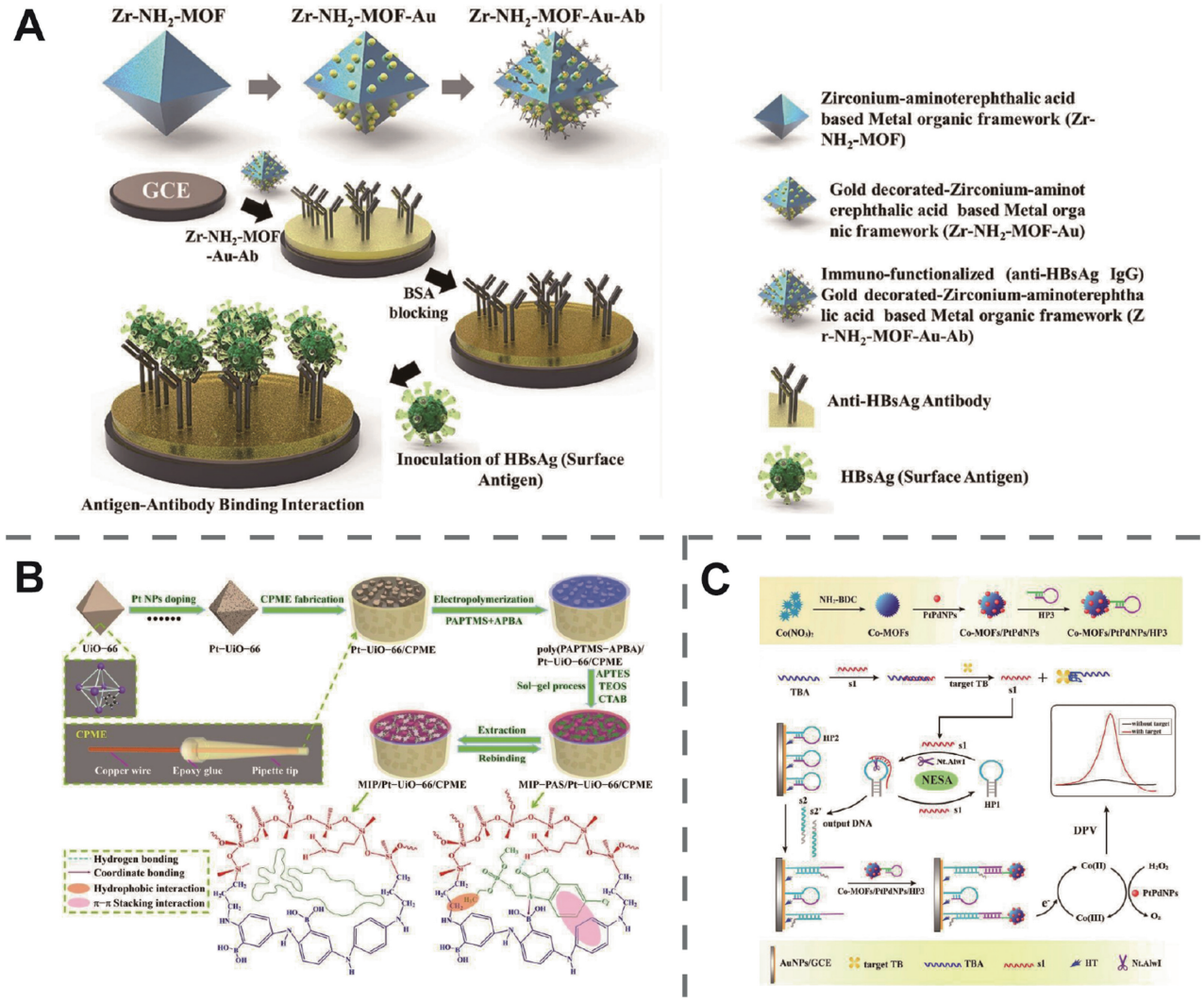

Fig. 3. (A) Schematic representation of the synthesis of Au@UiO-66(NH_2)-based immuno-electrochemical sensing for the detection of hepatitis B virus surface antigen. Reproduced with permission [68]. Copyright 2021, Springer. (B) Schematic illustration of the fabrication of MIP/Pt-UiO-66/CPME and MIP-PAS/Pt-UiO-66/CPME and their molecular structure. Reproduced with permission [76]. Copyright 2020, Royal Society of Chemistry. (C) Schematic illustration of the preparation of Co-MOFs/PtPdNPs/HP3 and the detection principle for thrombin. Reproduced with permission [94]. Copyright 2017, American Chemical Society.

Bimetallic alloys are also be applied as electrocatalysts owing to synergies between the physical and chemical characteristics of involving metals. More detailed, noble metals can be combined with either noble or base metals. As a result, bimetallic NPs can be used to synthesize desirable electrocatalysts in electrochemical sensing, such as PtPd NPs [94,95], AuPd NPs [96–98], AgPd NPs [99], AgPt NPs [100], AuCu NPs [101,102], AuPt NPs [103] and NiPd NPs [104]. For instance, Yang *et al.* fabricated an enhanced target-triggering nicking enzyme signaling amplification approach as signal amplifier. By doing so, they could prepare an ultrasensitive electrochemical biosensor for thrombin (TB) detecting associated with PtPd NPs embellished electroactive Co-based MOFs (Co-MOFs/PtPdNPs) as a redox mediator (Fig. 3C) [94]. The created Co-MOFs could be employed not only as carriers for immobilizing PtPd NPs, but also as signal tags without the addition of redox mediators. Simultaneously, when H_2O_2 was present, PtPd NPs constructed on Co-MOFs functioned as a horseradish peroxidase, catalyzing the oxidizing of H_2O_2 and accelerating the transformation of Co^{2+} to Co^{3+}, hence increasing the electrochemical signal. Based on above conception, the TB biosensor had high stability, repeatability, specificity and sensitivity in the region of 1 pmol/L to 30 nmol/L, with a LOD of 0.32 pmol/L. Wang *et al.* prepared a sensitive electrochemical aptasensor by applying Au@MoS_2/rGO nanocomposite and AuPd@Fe-MOFs to sensitive detect Pb^{2+} [96]. DNAzyme, which consisted of substrate chain (Apt1) and catalytic chain (Apt2), was applied to propose the aptasensor. Au@MoS_2/rGO nanocomposite was employed for the immobilization of the mercapto-group-labeled Apt1. Simultaneously, Apt2 was labeled with AuPd@Fe-MOFs, and Apt2 showed good catalytic ability for H_2O_2. When Pb^{2+} was present, the Apt1 of the DNAzyme was cut off catalytically, with the amount of AuPd@Fe-MOFs lowering. To achieve Pb^{2+} detection, the current response was connected to the concentration of Pb^{2+}. Because AuPd NPs had catalytic activity, the linear response of electrochemical sensor spanned from 5.0 pmol/L to 2.0 μmol/L, achieving a LOD of 0.07 pmol/L.

MNPs and MOFs both function as active sites. Apart from stabilizing MNPs, some MOFs containing transition metal node, such as Co [105–109], Ti [110,111], Ag [112], Fe [113], and Cu [114,115] ions or particular ligands [116–118] have excellent electrocatalytic activity in electrochemical sensing. MOFs can operate as the active center in addition to MNPs as the active site when it comes to these composites employed as electrochemical catalysts as for electrochemical sensing. For instance, porous PtNPs@Co(II)MOFs@PtNPs nanocomposites with great redox and catalytic performance were

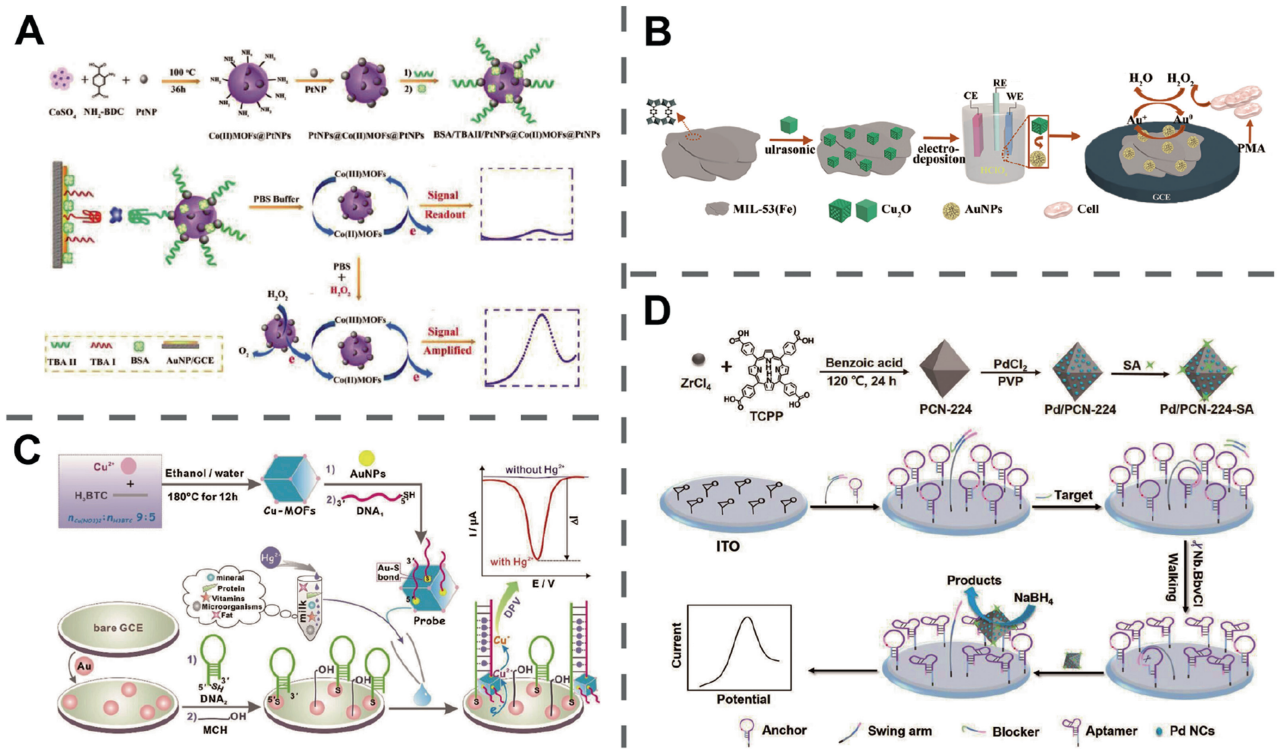

Fig. 4. (A) Principle description of preparation of TBA II bioconjugates and the signal amplification of thrombin detection. Reproduced with permission [109]. Copyright 2017, Elsevier. (B) Schematic illustration of the preparation process of Au@Cu_2O-MIL-53(Fe) for real-time monitoring of H_2O_2 released from the living cells. Reproduced with permission [113]. Copyright 2021, Springer. (C) Schematic illustration of the probe design and the DNA sensor for Hg^{2+} assay using the optimal Cu-MOFs as signal output and T-Hg^{2+}-T coordination chemistry. Reproduced with permission [114]. Copyright 2020, Elsevier. (D) Schematic illustration of the preparation of an immunosensor based on Pd/PCN-224-SA and construction of DNA walker substrate on the indium tin oxide (ITO) electrode. Reproduced with permission [116]. Copyright 2018, American Chemical Society.

developed by Yang *et al.* for use in an electrochemical aptasensor to achieve TB detection (Fig. 4A) [109]. Inner PtNPs were encased by aminofunctionalized Co(II)MOFs, and then more PtNPs were deposited on Co(II)MOFs@PtNPs surface through the Pt-N link, resulting in constituting PtNPs@Co(II)MOFs@PtNPs nanocomposite. This unique structure not only offered a conduit for electron transmission, but also enhanced the surface area, allowing for the loading of a significant amount of TBA II. Furthermore, the PtNPs@Co(II)MOFs@PtNPs nanocomposites might be employed directly as redox labels for charge creation due to the electron shift from Co(II) to Co(III). In addition, when H_2O_2 was present, the composites catalyzed H_2O_2 oxidation could promote the electronic transfer of Co(II) to Co(III), issuing in amplifying electrochemical signal. Based on the foregoing excellent benefits, TB was detected at concentrations ranging from 0.1 pmol/L to 50 nmol/L with a LOD of 0.33 fmol/L. Chen *et al.* produced a Cu_2O-mediated Au nanoparticle grown on MIL-53(Fe) ternary nanocomposite for real-time hydrogen peroxide monitoring. Redox assembly method was applied to synthesize Cu_2O-MIL-53(Fe), which provided the active sites for $AuCl_4^-$ (Fig. 4B) [113]. The Au@Cu_2O-MIL-53(Fe)/GCE biosensor was created by electrochemically depositing nano-Au evenly on the surface of Cu_2O. Attributed to the synergistic impact among AuNPs, Cu_2O, and MIL-53(Fe), the hybrid nanocomposite demonstrated superior electrochemical characteristics as electrode materials when compared to individual components. It showed that both Au and Cu_2O-MIL-53(Fe) presented a satisfactory catalytic activity towards H_2O_2 by electrochemical measurement with a LOD of 1.01 μmol/L in the linear range of 10–1520 μmol/L. Zhang *et al.* designed a facile sensor for electrochemical analysis of Hg^{2+} in dairy products (Fig. 4C) [114]. Since Hg^{2+} and thymine (T)-rich DNA strands could be uniquely identified by using the best Cu^{2+}-based MOFs as signal recording, interferences induced by milk matrices could be efficiently removed. AuNPs were successfully grown on Cu-MOFs and had the ability to boost sensitivity by speeding up electron transfer. Cu-MOFs were demonstrated to be an effective supporter for loading AuNPs for probe building, as well as an electroactive species for signal construction. This sensor, in contrast to earlier approaches, substantially simplified the electrochemical measuring process and allowed for extremely sensitive, selective, and quick examination of Hg^{2+} with a LOD of 4.8 fmol/L.

MOFs can be endowed with catalytic properties by the presence of some ligands, which should not be disregarded. For example, Yan *et al.* established a dual signal amplification approach for sensitive electrochemical biosensing by combining Pd/MOF electrocatalysis with DNA walker-induced conformation switch (Fig. 4D) [116]. Signal tags were created the by decreasing the Pd precursor on the PCN-224 surface to constitute Pd/PCN-224 composite, then conjugating it with the recognition element streptavidin. Owing to the porphyrin linkers had redox activity, both MOF and Pd NPs could catalyze $NaBH_4$ oxidation. The tandem signal amplification system, as the system that finally detected target DNA, displayed good performance, including a wide detection range of 100 fmol/L–100 nmol/L, a low detection limit of 33.6 fmol/L, and effective discriminating against single-base mismatched oligonucleotide. Wang *et al.* introduced a new postsynthetic modification followed by ion-exchanging to integrate either pore-restricted Ag NPs or immobilized Ag^+ ions into porphyrinic Zr-MOFs with redox activity [117]. The size of the Ag NPs or framework-immobilized Ag(I) ions generated was restricted to 3 nm. Since both Ag NPs and the porphyrinic linkers in NU-902 electrocatalyzed for nitrite oxidation, the resulting composites could be used as in electrochemical nitrite sensing, with a linear range of up to 2.0 mmol/L and a LOD

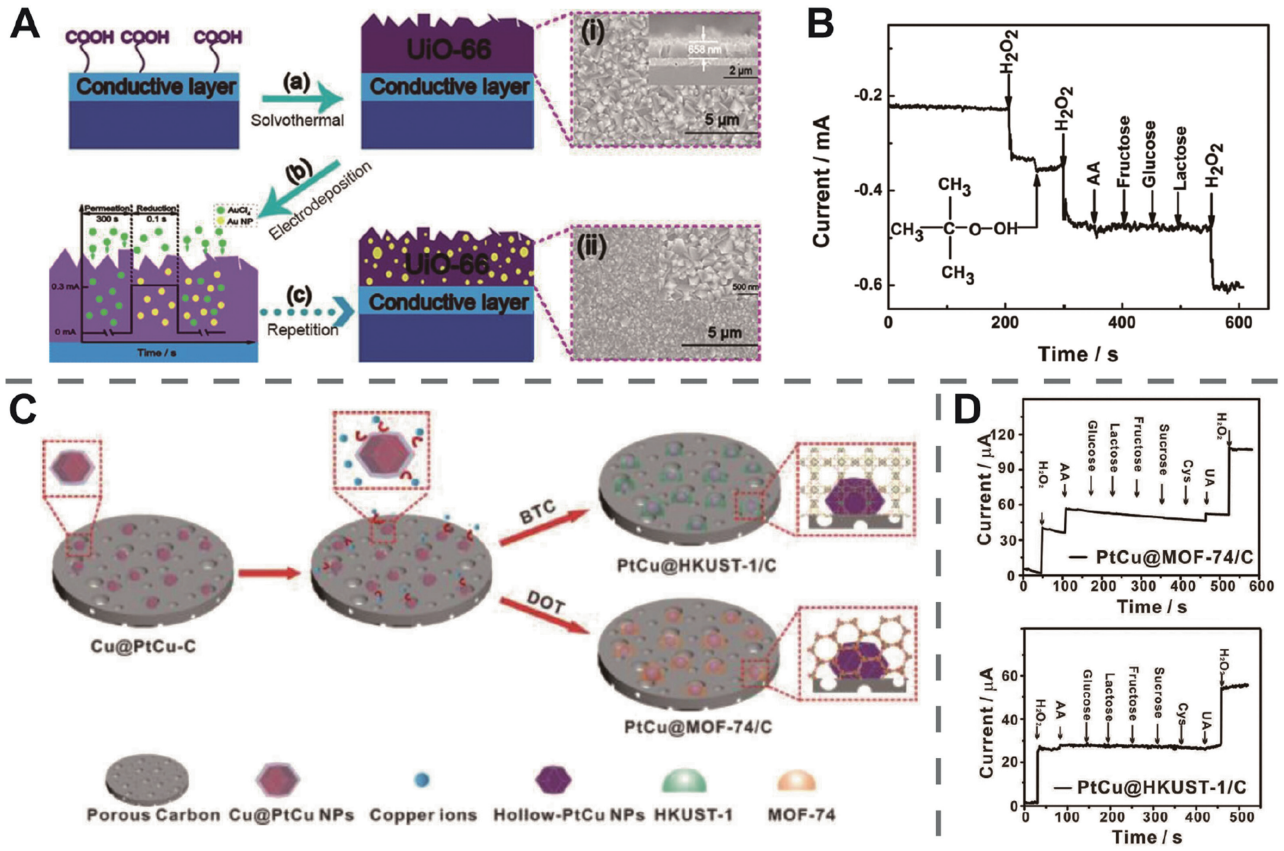

Fig. 5. (A) Schematic illustration of the fabrication process of the Au NPs/UiO-66 film: (a) solvothermal, (b) electrodeposition, and (c) repetition. Insets show the top-view SEM images of the surface of the UiO-66 film (i) and Au NPs/UiO-66 film (ii) and the cross-sectional SEM image of the UiO-66 film (inset of (i)). (B) Current response of the 50-Au NPs/UiO-66 film to 0.5 mmol/L H_2O_2 in the presence of 0.5 mmol/L TBHP, AA, fructose, glucose, and lactose is shown. (A, B) Reproduced with permission [119]. Copyright 2021, American Chemical Society. (C) Schematic illustration of the synthesis of PtCu@MOFs supported on PC. (D) Current response of PtCu@MOF-74/C (Top) and PtCu@HKUST-1/C (Bottom) to 50×10^{-6} mol/L H_2O_2, AA, glucose, α-lactose, D-fructose, sucrose, L-cysteine, and UA at +0.4 V (*vs.* SCE) in a 0.1 mol/L PBS solution (pH 7.4). (C, D) Reproduced with permission [120]. Copyright 2018, Wiley.

of 9.1 μmol/L, substantially better than the original porphyrinic Zr-MOF.

MNPs function as active sites, and MOFs with high porosity control size selectivity. Due to its inherent porosity, MOFs may transmit/adsorb reactants with high selectivity, limiting their passage to MNPs and preventing unwanted molecules from flowing beyond the pore size of the MOFs. Their composites with synergy show excellent selectivity and anti-interference properties, making it a promising candidate for non-enzymatic electrochemical sensors [119–122]. For example, an electrocatalytic active film on the surface of an electrode containing Au nanoparticles embedded in a metal-organic framework (UiO-66) film was presented by Wang *et al.* to detect H_2O_2 (Fig. 5A) [119]. Apart from acting as protective skeletons, the UiO-66 film (0.6 nm) possessed a favorable anti-interference property, which could be attributed to the UiO-66 film's appropriate triangular opening channel, which prevented macromolecules from reaching the encapsulated Au NPs surface and had a splendid selectivity for H_2O_2. H_2O_2 diffused swiftly through the UiO-66 shell, making catalysis of H_2O_2 reduction easier. Even if interferents (*e.g.*, TBHP, AA, fructose, glucose and lactose) had the same concentration as H_2O_2, the current response to interferents was negligible due to the anti-interference ability of composites (Fig. 5B). The resulting sensor had a 200–23,000 mmol/L linear response range, achieving a LOD of 0.045 mmol/L simultaneously. Chen *et al.* produced PtCu@MOF-74 and PtCu@HKUST-1 successively, then examined their effectiveness in selective H_2O_2 reduction electrocatalytically (Fig. 5C) [120]. MOF-74 and HKUST-1 had 1.1 nm and 0.6 nm pore diameters, respectively. The pore sizes of MOF-74 and HKUST-1 were 1.1 nm and 0.6 nm, respectively. PtCu@HKUST-1 had superior selectivity than PtCu@MOF-74 due to its smaller MOF pore size (Fig. 5D). Although the concentration of ascorbic acid was 100 times greater than the target hydrogen peroxide, PtCu@HKUST-1 exhibited strong anti-interference performance. PtCu@HKUST-1 detected H_2O_2 with a LOD of 0.22 mmol/L on account of its remarkable anti-interference performance.

To conclude, the congenerous principles of MNPs/MOFs composites applied in electrochemical sensing are demonstrated below: (1) Several composites can be employed as support platforms for effectively biomolecules immobilization attributed to their highly porous structure, broad surface areas, and satisfying biological affinity; (2) Partial composites possess high catalytic performance, preeminent electrical conductivity, and good stability, allowing them to efficiently catalyze reactions and produce observable electrochemical signals. Due to the synergistic impact between MNPs and MOFs, electrochemical sensors on the basis of MNPs/MOFs composites exhibit higher sensitivity, stability, and efficiency, and offer great application prospects.

2.2. Fluorescent sensors

Because of their unique and programmable fluorescence features, MNPs/MOFs composites are also employed as platforms for fluorescence sensing. MNPs/MOFs composite-based fluorescence sensors typically use one of two sensing techniques. The target molecule can quench the fluorescence intensity of MNPs/MOFs

Table 2
Fluorescent sensors based on MNPs/MOFs composites.

Nanomaterial	Analyte	Linear response range	Detection limit	Ref.
CDs/AuNCs@ZIF-8	Copper(II) ions	10^{-3}–10^{3} μmol/L	0.3324 nmol/L	[127]
AuNCs@NMOFs	Hypochlorite	80 nmol/L–1.0 μmol/L	0.96 μmol/L	[128]
AuNCs@ZIF-8	Bilirubin	0.1–5.0 μmol/L	0.07 μmol/L	[129]
AuNCs@ZIF-8	3-Nitrotyrosine	5–200 nmol/L	1.8 nmol/L	[130]
Cu NCs@GSH/MOFs	–	–	–	[131]
AuNCs/MIL-68(In)-NH_2/Cys	Hg^{2+}	20 pmol/L–0.2 μmol/L 0.2–60 μmol/L	6.7 pmol/L –	[132]
AgNCs-BSA@ZIF-8	Cu^{2+}	4.0×10^{-4}–160 μmol/L	0.1 nmol/L	[133]
AgNPs@ZnMOF	Patulin	0.1–10 μmol/L	0.06 μmol/L	[134]

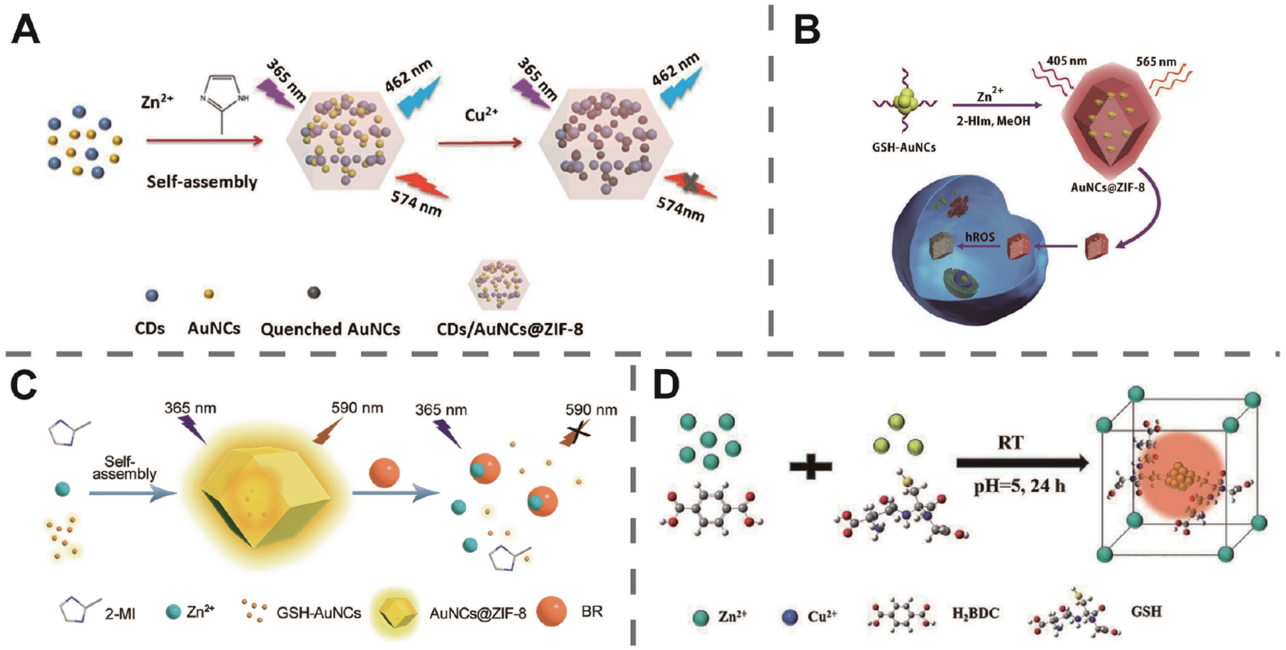

Fig. 6. (A) Schematic illustration of the strategy for the detection of Cu^{2+}. Reproduced with permission [127]. Copyright 2020, Springer. (B) Schematic illustration of synthesized AuNCs@NMOFs nanocomposites and hROS detection in living cells. Reproduced with permission [128]. Copyright 2019, Elsevier. (C) Schematic illustration of the sensing mechanism of bilirubin by AuNCs@ZIF-8. Reproduced with permission [129]. Copyright 2021, Royal Society of Chemistry. (D) Schematic illustration of the one-pot synthesis of CuNCs@GSH/MOF-5 composites. Reproduced with permission [131]. Copyright 2018, Royal Society of Chemistry.

composites with intrinsic fluorescence, and the concentration of the target molecule can be measured based on the quenching degree. MNPs/MOFs composites can also be utilized to catalyze in the creation of fluorescent products, resulting in fluorescent signals corresponding to the concentration of interest. Applications of MNPs/MOFs composites as for fluorescence sensor are addressed below, based on its sensing approach (Table 2).

It is notable that some MNCs have distinctive luminous capabilities [123–125]. However, in fluorescence sensing applications, their limited environmental durability and weak quantum yield offer substantial hurdles [126]. By intergrating MNCs with porous MOFs, we can create MNCs/MOFs composites to overcome the above concerns since the increased durability and luminescent efficiency of MNCs.

In order to enhance the fluorescence intensity and stability of NCs by utilizing the porosity of MOFs, several studies have been published in relation to the encapsulation of metal NCs featuring fluorescence and other nanomaterials into MOFs. A dual-emission MOF based ratiometric fluorescence nanoprobe was presented by Tan *et al.* for Cu^{2+} detection (Fig. 6A) [127]. Carbon dots (CDs) and gold nanoclusters were implanted into zeolitic imidazolate framework-8 (ZIF-8) to stabilize them, and then CDs/AuNCs@ZIF-8 composited with dual-emission peaks when producing UV excitation. The fluorescence attributable to AuNCs could be swiftly quenched in the presence of Cu^{2+}, whereas the fluorescence of CDs functioned as a reference with alterations difficult to detect. As a result, the prepared CDs/AuNCs@ZIF-8 composites were used as sensitive and selective ratiometric fluorescent nanoprobes to detect Cu^{2+}. With a LOD of 0.3324 nmol/L, the synthetic sensing system was proven to be able to detect Cu^{2+} at concentrations ranging from 10^{-3} to 10^{3} μmol/L. Cao *et al.* successfully encapsulated glutathione stabilized gold nanoclusters (GSH-AuNCs) in nanoscale metal-organic frameworks (NMOFs) (Fig. 6B) [128]. In comparison to GSH-AuNCs, the AuNCs@NMOFs demonstrated a nearly 10-fold increase in fluorescence intensity and a 10-fold longer fluorescence lifespan. Highly reactive oxygen species (hROS) quenched the fluorescence intensity of AuNCs@NMOFs because of their high oxidation capacity. The nanocomposites were employed to detect hROS with a proportional band of 80 nmol/L to 1.0 mmol/L and a LOD of around 30 nmol/L toward hypochlorite (as a representation of hROS).

MOFs can limit the freedom of mobility of MNC in MNCs/MOFs composites, allowing MNCs to remain aggregated, resulting in aggregation-induced emission and improved quantum yield. A fluorescence analysis approach was developed by Xia *et al.* for exceptionally sensitive bilirubin detection on the strength of AuNC and MOF composites (AuNCs@ZIF-8) (Fig. 6C) [129]. The confinement effect of the ZIF-8 resulted in an aggregation-induced emis-

sion enhancement, and co-precipitation of AuNCs@ZIF-8 was effective. When compared to Au NCs, the quantum yield of the product was raised by nearly 7.0 times, and the fluorescence lifetime was increased from 2.29 μs to 11.51 μs. When bilirubin was mixed with Zn^{2+} from ZIF-8, the configuration of composites was damaged, AuNC changed from aggregated to scattered, with fluorescence intensity considerably reduced. Bilirubin detection therefore had linear range of 0.1–5.0 μmol/L, with a detection limit of 0.07 μmol/L. In addition, Jalili *et al.* created a new greatly fluorescent hybrid material (AuNCs@ZIF-8) by enclosing AuNCs in the zeolitic imidazolate framework [130]. The quantum yield of hybirds reached 36.6%, roughly 15 times that of solitary AuNCs, thanks to confinement-assisted emission amplification. AuNCs@ZIF-8 composites as-obtained were utilized to create a 3-nitrotyrosine sensor, which was ultrasensitive and extremely selective. When compared to plain AuNCs sensing without the amplification effect of ZIF-8, the produced sensor based on AuNCs@ZIF-8 exhibited a range of 5–200 nmol/L and a detection limit of 1.8 nmol/L. In another example, Han *et al.* presented a one-pot synthesis of glutathione (GSH) modified Cu NCs (Cu NCs@GSH) and MOF-5 to constitute Cu NCs@GSH/MOFs (Fig. 6D) [131]. By using the cavities of the inflexible confining scaffold of MOF-5 to ensure the stability of GSH decorated Cu NCs, the fluorescence intensity was increased by nearly 35 times and the stability was prolonged at least 30 times. Furthermore, the prepared Cu NCs@GSH/MOFs hybrids were sensitive to pH changes and their fluorescence emission shifted from blue to orange to red in a reversible manner.

The quantum yield of MNCs is improved *via* energy/electron transmission from particular ligands in MOFs to MNCs according to prior research. For instance, Wu *et al.* used increased dual emissions from glutathione stabilized Au NCs/indium-based MOF decorated with cysteine (AuNCs/MIL-68(In)-NH_2/Cys) to produce ratiometric fluorescent sensors for Hg^{2+} detection [132]. With AuNCs equally dispersed on MIL-68(In)-NH_2, the resulting sensor showed dual fluorescence emissions at 438 and 668 nm respectively under 370 nm excitation, which were attributable to MIL-68(In)-NH_2 and GSH-AuNCs. The red fluorescence peak at 668 nm was quenched when Hg^{2+} was present, while the blue peak at 438 nm was somewhat modified. The Hg^{2+} detection for the synthesized AuNCs/MIL-68(In)-NH_2/Cys sensor ranged from 20 pmol/L to 0.2 μmol/L and 0.2 μmol/L to 60 μmol/L, respectively. Additionally, Fan *et al.* coated silver nanoclusters (AgNCs) with bovine serum albumin (BSA) and then used a protein-mediated biomineralization method to encapsulate them in porous ZIF-8 [133]. The fluorescence intensities of the AgNCs-BSA@ZIF-8 nanocomposites were found to be consistently higher than expected during the BSA covering and ZIF-8 encasement phases. The produced nanocomposites might have a particular accumulation and sensitive reaction to Cu^{2+}, causing the reasonable dampening of their fluorescence intensities. The fluorescent sensing system was found to detect Cu^{2+} with a linearity range of 0.4 nmol/L–160 μmol/L, accomplishing a LOD of 0.10 nmol/L.

Apart from the aforementioned, MNPs/MOFs composites can accelerate processes to create fluorescent compounds, resulting in observable fluorescent signals. AgNPs@ZnMOF with high peroxidase-mimetic property was utilized as a foundation for molecularly imprinted polymer (MIP) to selectively detect patulin without interference from other comparable chemicals [134]. Researchers constructed AgNPs@ZnMOF by installing Ag NPs into the nanopores of ZnMOF. The increased surface areas of MOF significantly boosted the catalytic performance of Ag NPs. They discovered afterwards patulin could restrain the catalytic activity of AgNPs@ZnMOF. As a result, a reliable patacillin probe was created by combining selective recognition properties of MIP with the new AgNPs@ZnMOF nanocomposite which featured outstanding peroxide-like activity and a sensitive fluorescence detection system. The H_2O_2-terephthalic acid reaction was catalyzed by the MIP-capped AgNPs@ZnMOF, which created a high fluorescent product and followed by an exceptional fluorescence signal. The fluorescence intensity was proportionally connected to patulin content ranging from 0.1 to 10 μmol/L with a LOD of 0.06 μmol/L when patulin was present.

In conclusion, MNPs/MOFs composites exhibiting synergistic effects seek to boost the fluorescence signal of fluorescence sensors. Restricted effect of MOFs on MNPs, stabilizing function of MOFs or energy/electron shifting from some specific MOF ligands to MNPs, are all responsible for the fluorescence increase signals.

2.3. Colorimetric sensors

MNPs/MOFs composites in large amounts exhibit approximated enzyme-like catalytic performance and are able to efficiently accelerate chromogenic chemical processes to yield products showing colors. Colorimetric sensors to detect diverse analytes are frequently developed through catalytic processes accompanied by prominent color changes. As a result, a discussion of the colorimetric applications of several MNPs/MOFs composites is provided (Table 3).

2.3.1. Dispersion of MNPs by MOFs to enhance catalytic activity

In accordance with previous reports, Au NPs [135–137], Ag NPs [138] and Pt NPs [139,140], known as noble-metal NPs, perform interesting peroxidase-like activity. Furthermore, MNPs are dispersed uniformly and their catalytic efficiency is also improved by adding MOFs. A simple and ultrasensitive colorimetric probe on the basis of the peroxidase-like activity of Ag NPs/flake-like Zn MOF nanocomposites was devised by Bagheri *et al.* for the detection of dangerous peroxide explosives [138]. Silver nanoparticles were constituted into the tiny pores of the Zn MOF during the production progress of Ag@ZnMOF. The nanocomposite, which was evaluated to be a peroxidase mimic based on H_2O_2 oxidations, had a synergetic and increased catalytic activity thanks to high reactive AgNPs and large surface area of MOFs. The technique development was used to identify triacetone triperoxide (TATP), one of the most dangerous peroxide explosives. Under acidic conditions, TATP was degraded to produce H_2O_2, and subsequently 3,3′,5,5′-tetramethylbenzidine (TMB) was oxidized by H_2O_2 to generate oxTMB (a well-known blue colored charge transfer complex) in the presence of Ag@ZnMOF as the reaction catalyst. The absorption intensity of the generated blue solution and the TATP content were found to have a linear relationship in the 0.4–15 mg/L range, with a LOD of 0.1 mg/L. Wang *et al.* created a porous and chemically stable zirconium-based metal-organic framework named as UiO-66, which was applied to manufacture Pt/UiO-66 nanocomposites (Fig. 7A) [139]. UiO-66 was selected as a carrier attributable to its additional features of strong acid/base media stability and the capacity to donate electrons. Due to the confinement effect of mesopores, the produced Pt/UiO-66 composites maintained an excellent dispersion of ultra-small Pt particles of 3.8 nm in the whole UiO-66. Pt/UiO-66 composites exhibited highly efficient oxidase and peroxidase performances, which were both dependent on the amount of platinum. The development of Pt/UiO-66 was intended to improve the efficiency and durability of Pt NPs while also providing additional active sites for catalytic processes. Employing the peroxidase-mimetic activity of Pt/UiO-66, a selective and sensitive colorimetric approach that was be applied to detect glucose was devised with a linearity range of 0.1–1.33 mmol/L and a LOD of 0.033 mmol/L.

2.3.2. MOFs act as catalysts

Several MOFs can stimulate catalytic activity of enzyme in addition to their protective effects. In particular, peroxidase-like activ-

Table 3
Colorimetric sensors based on MNPs/MOFs composites.

Nanomaterial	Analyte	Linear response range	Detection limit	Ref.
Au@ZIF-67	Cysteine	0–800 μmol/L	0.5 μmol/L	[135]
Hemin-Au@MOF	Alpha-fetoprotein	0.080–43 ng/mL	0.020 ng/mL	[136]
AuNP@MOF	Hg^{2+}	200–400 pmol/L	103 pmol/L	[137]
Ag@ZnMOF	Triacetone triperoxide	0.4–15 mg/L	0.1 mg/L	[138]
Pt/UiO-66	Glucose	0.1–1.33 mmol/L	0.033 mmol/L	[139]
Pt NPs@UiO-66-NH_2	Hg^{2+}	0–10 nmol/L	0.35 nmol/L	[140]
TBA-Pt-MOF	Thrombin	0.5 pmol/L–1 nmol/L	0.17 pmol/L	[141]
Fe-MIL-88-Pt	Chloramphenicol	0.1–1000 pmol/L	0.03 pmol/L	[142]
Pt/Fe-MOF	Glucose	0–400 μmol/L	2.3 μmol/L	[143]
	H_2O_2	20–600 μmol/L	13.01 μmol/L	
Fe_3O_4@MIL-100(Fe)	Cholesterol	2–50 μmol/L	0.8 μmol/L	[144]
FePt@MOFs	H_2O_2	40–800 μmol/L	18.9 μmol/L	[145]
Pt/NH_2−MIL-101	Dopamine	1–60 μmol/L	0.42 μmol/L	[146]
NH_2−MIL-125(Ti)	H_2O_2	2–10 μmol/L	0.24 μmol/L	[147]
	Cysteine	1–10 μmol/L	0.14 μmol/L	
	Hg^{2+}	1–5 μmol/L	100 nmol/L	
MVCM@Pt	Visfatin	1–100 ng/mL	0.11 ng/mL	[148]
UsAuNPs/2D MOF	Trichlorfon	1.7–42.4 μmol/L	1.7 μmol/L	[149]
PtNPs/Cu-TCPP(Fe)	H_2O_2	20–600 μmol/L	2.3 μmol/L	[150]
	Glucose	3.9–6.4 μmol/L	0.24 μmol/L	
GOx&AuNCs@ZIF-8	Glucose	1.0–25.0 μmol/L	0.5 μmol/L	[151]

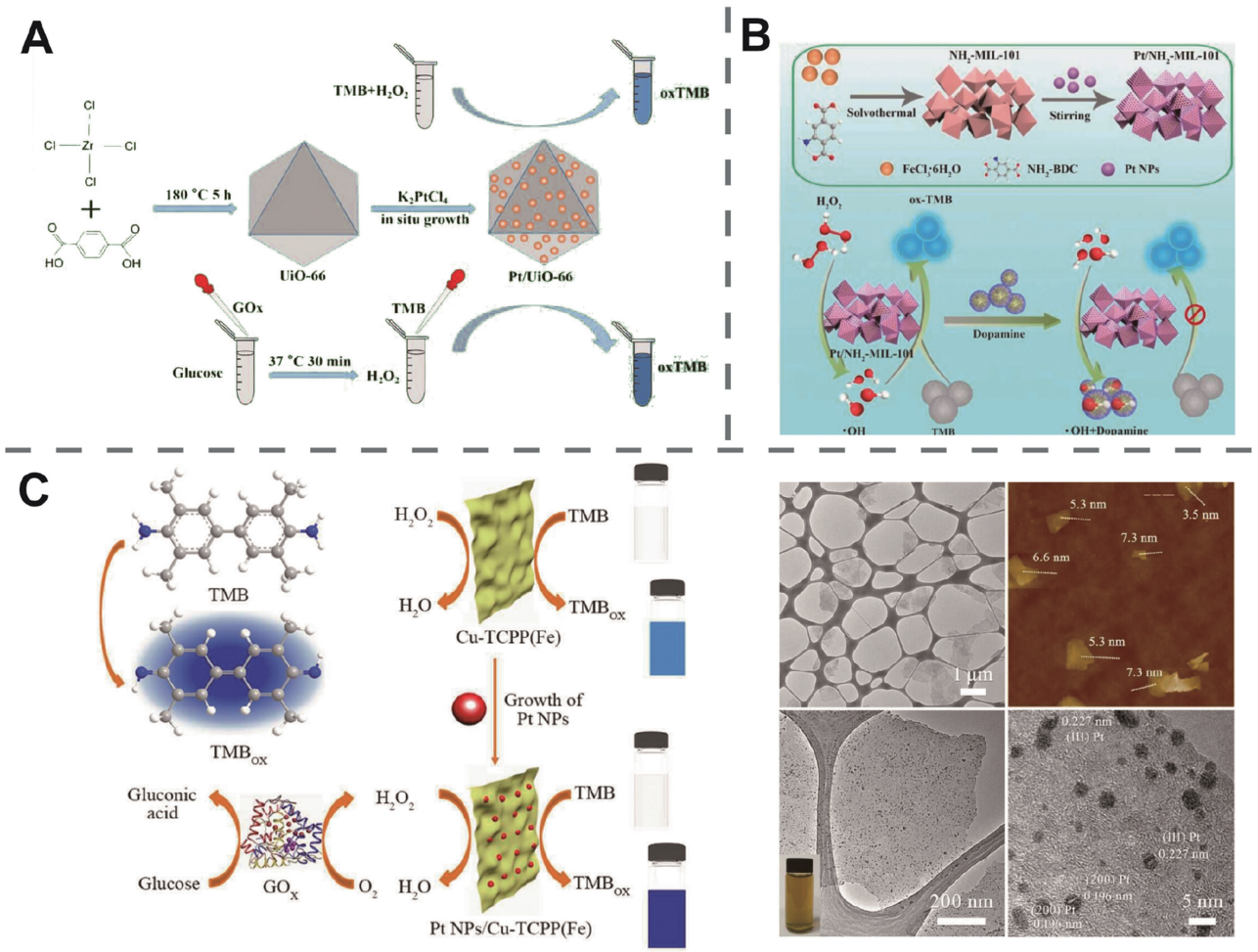

Fig. 7. (A) Schematic illustration for the preparation of the Pt/UiO-66 hybrid nanozymes and detection of glucose. Reproduced with permission [139]. Copyright 2021, American Chemical Society. (B) Schematic illustration of the synthesis of Pt/NH_2−MIL-101 and the detection of dopamine. Reproduced with permission [146]. Copyright 2021, MDPI. (C) Schematic illustration of the synthesis of Pt/Cu-TCPP(Fe) composites and their application in the colorimetric detection of H_2O_2 and glucose. Low-magnification TEM image of Cu-TCPP(Fe) nanosheets. AFM image of Cu-TCPP(Fe) nanosheets. TEM image of PtNPs/Cu-TCPP(Fe) hybrid nanosheets. Inset: Photograph of the PtNPs/Cu-TCPP(Fe) hybrid nanosheets solution. HRTEM image of PtNPs/Cu-TCPP(Fe) hybrid nanosheet. Reproduced with permission [150]. Copyright 2018, American Chemical Society.

ity has been observed in MOFs containing transition metal ions, such as Fe-MOF [141–146], Ti-MOF [147] and Ce-MOF [148]. Li *et al.* used the hydrothermal approach to develop uniformly dispersed NH_2−MIL-101 with an octahedral structure, and then established coordinating bonds with Pt NPs to synthesize Pt/NH_2−MIL-101 with a bimetallic catalytic core (Fig. 7B) [146]. The development of bimetallic centers and the large specific surface area of NH_2−MIL-101 could enhance the number of catalytic centers. In addition, potential difference between Fe and Pt was large enough to enable electron shift, thus improving catalytic performance. As a result, the peroxidase-mimetic activity of obtained Pt/NH_2−MIL-101 was enhanced by 1.5 times. Moreover, Pt/NH_2−MIL-101, which possessed remarkable peroxidase performance, were capable of rapidly catalyzing the decomposition of H_2O_2 to generate hydroxyl radical (•OH), thus altering the color of TMB. In the presence of dopamine, the •OH generated by competition with TMB, the hue changed dramatically when the blue ox-TMB was converted to colorless TMB. For concentrations ranging from 1 μmol/L to 60 μmol/L, a linearity connection between absorbance intensity and DA concentration was discovered, with a LOD of 0.42 μmol/L. Zhang *et al.* connected impregnation with borohydride reduction procedures to produce Au@NH_2−MIL-125(Ti) composites successively, then they successfully deposited small and uniform Au NPs on composites surface and captured them in the NH_2−MIL-125(Ti) nanocages [147]. The resultant nanohybrid nanozyme outperformed individual Au NPs and NH_2−MIL-125(Ti) in terms of peroxidase-mimetic catalytic activity. The enhanced peroxidase-mimetic activity of Au NPs and NH_2−MIL-125(Ti) was ascribed to their synergistic mechanisms. Besides, compared with natural horseradish peroxidase, the K_m values for TMB and H_2O_2 were lower, manifesting that both substrates demonstrated a higher affinity for the nanozyme. A multifunctional platform to detect H_2O_2 using colorimetric method, cysteine, and Hg^{2+} was developed based on these findings, with detection limits of 0.24 mmol/L, 0.14 mmol/L, and 100 nmol/L, respectively.

2.3.3. MNPs/MOFs for multi-enzyme systems

In addition, MNPs/MOFs composites possessing enzyme-mimetic activity can be used in multienzyme systems with other oxidases to accomplish cascade reactions [149–151]. For example, an easy and convenient method was devised by Chen *et al.* to manufacture two-dimensional MOF composites modified by PtNPs (Fig. 7C) [150]. Cu-TCPP(Fe) nanosheets with a thickness of less than 10 nm were employed to serve as a new platform for growing ultrasmall, homogeneous platinum nanoparticles. The resulting hybrid nanocomposites (PtNPs/Cu-TCPP(Fe)) demonstrated observably greater peroxidase-mimetic performance than single PtNPs, single Cu-TCPP(Fe) nanomaterials, and their hybrids synthesized physically because of the synergistic mechanism of the unique structure. Since PtNPs/Cu-TCPP(Fe) nanocomposites possessed peroxidase-mimetic activity, they were combined with glucose oxidase (GOx) to create a sensitive, fast, and selective cascade colorimetric technique for glucose measurement. The suggested sensing strategy was demonstrated to detect glucose concentrations in the range of 2–200 mmol/L with a LOD of 0.994 mmol/L. Chi *et al.* synthesized GOx&AuNCs@ZIF-8 composites with glucose oxidase and Au NCs co-encapsulated zeolitic imidazolate frameworks and employed it as a ultrasensitive colorimetric glucose sensor on the basis of the cascade reaction [151]. Glucose oxidase transformed glucose to gluconic acid and produced H_2O_2, which was employed by AuNCs to oxidize TMB, resulting in the colored oxTMB by oxidization. The catalytic activity of GOx and AuNCs@ZIF-8 solution was 19.3 times higher than that of free GOx/AuNCs solution under the same conditions, on account of the improved cascade reactions and protective impact arising from ZIF-8 shell on enzymes, and the glucose sensor demonstrated high selectivity and sensitivity. On account of the distinct cascade response, the glucose sensor exhibited an outstanding linear relationship with glucose concentrations ranging from 1.0 μmol/L to 25.0 μmol/L, with a LOD of 0.8 μmol/L.

To generate colorimetric data, colorimetric sensors founded on MNPs/MOFs composites typically utilize enzyme-like catalytic performance of MNPs/MOFs composites. In terms of the first colorimetric method, MOFs promote homogenous distribution of MNPs and ameliorate their superior catalytic performance, most of which possess peroxidase-mimetic activity. Secondly, in addition to protecting MNPs, certain MOFs exhibit enzyme-mimetic activity, and the synergistic action of these enzymes improves catalytic performance. Finally, cascade reactions can be generated using MNPs/MOFs composites with enzyme-like catalytic performance and additional oxidases.

2.4. Surface-enhanced Raman scattering sensors

Because of their electromagnetic processes, plasmonic nanoparticles are the first choice to construct surface-enhanced Raman scattering (SERS) substances. Unfortunately, because of the destabilization and low repeatability of typical surface-enhanced Raman scattering materials, their use in SERS sensing is constrained. Because of their porous architectures, MOFs not only tolerate homogeneously distributed MNPs, but also prohibit them from aggregating under adverse reaction conditions. Additionally, MOFs adsorb target molecules, promotes closeness to the MNP surface (surface-enhanced Raman scattering active sites) and enhances surface-enhanced Raman scattering signals. Therefore, MNPs/MOFs composites have earned great enthusiasms to create SERS substrates with superior stability and sensitivity. The researches that Au NPs, Ag NPs and their bimetallic NPs have been successfully encapsulated into MOFs to construct SERS substrates are summarized below (Table 4).

2.4.1. Au/MOFs

SERS detection of several target analytes has been achieved by utilizing composites comprising SERS-active Au NPs and MOFs [152–161]. An *in-situ* reduction approach was applied by Wang *et al.* to make Au NPs adorned amino-functionalized Cr-based MOFs [NH_2−MIL-101(Cr)@Au] as a SERS substrate to adsorb simultaneously and detect acid orange II (AO II) [156]. Due to their three-dimensional structure, extremely large specific surface areas along with countless amino groups, Au NPs were closely and equably modified on NH_2−MIL-101(Cr) surface, allowing for more precise identification as well as unsaturated sites, thus delivering a significant pre-concentration impact on SERS signals amplification. These NH_2−MIL-101(Cr)@Au composites demonstrated selective and strong adsorption performance for AO II and effectively detected AO II with a wide detection range of 0.05–50 mg/L and a low detection limit of 0.05 mg/L with good sensitivities.

Due to the size selectivity of MOF shell, partial MNPs/MOFs composites are especially suitable for selective SERS detection. For example, Pu *et al.* created MNP@Au@MIL-100(Fe) substrates with SERS activity by using a magnetic nanoparticle (MNP) as the core, which was uniformly embellished with Au NPs, and then coating it with a MOF shell of MIL-100(Fe), which functioned as a molecular sieve, allowing only appropriately sized molecules to get access to the internal AuNP, so as to prevent disturbance (Fig. 8A) [160]. Magnetic nanoparticles in the MNP@Au@MIL-100(Fe) substrate could aid SERS active nanoparticles in producing denser and more homogeneous hot spots and avoid aggregating, while uniform mesoporous windows (5.0 and 8.6 Å) in MOF allowed the substrate to sieve macromolecules with selectivity (Fig. 8B). As a consequence, food matrix interference was prevented, and quantitative analytical capability was considerably enhanced. The devel-

Table 4
SERS sensors based on MNPs/MOFs composites.

Nanomaterial	Analyte	Linear response range	Detection limit	Ref.
AuNP/AE-MIL-101 (Cr)	Carboxylesterase 1	0.1–120 ng/mL	6.7×10^{-13} mol/L	[152]
AuNPs/MIL-101(Cr)	Benzidine	2.0–20.0 μg/L	0.21 μg/L	[153]
	4-Aminobiphenyl	1.0–15.0 μg/L	0.23 μg/L	
AN@ZIF	4-Nitrobenzenethiol	–	–	[154]
Au@ZIF-8	Putrescine	0–10^{-4} (v/v)	76.99 ppb	[155]
	Cadaverine	0–10^{-4} (v/v)	115.88 ppb	
NH_2−MIL-101(Cr)@Au	Acid orange II	0.05–50 mg/L	0.05 mg/L	[156]
UiO-66(NH_2)@Au	New coccine	1–50 mg/L	0.4015 mg/L	[157]
	Orange II	0.1–50 mg/L	0.0546 mg/L	
UiO-66/AuNPs	Heterocyclic amine	2.0–200.0 μg/L	1.18 μg/L	[158]
	Sudan dye	1.0–200 μg/L	0.49 μg/L	
AuNPs/MIL-101	*p*-Phenylenediamine	1.0–100.0 ng/mL	–	[159]
	Alpha-fetoprotein	1.0–130.0 ng/mL	–	
MNP@Au@MIL-100(Fe)	Malachite green	–	0.132 nmol/L	[160]
Au NBP/end-ZIF	4-Aminothiophenol	–	10^{-8} mol/L	[161]
Au NBP@ZIF	–	–	–	
Au NBP/waist-ZIF	–	–	–	
AuNPs@MIL-101@GOx	Glucose	10−200 μmol/L	4.2 μmol/L	[162]
AuNPs@MIL-101@LOx	Lactate	0−200 μmol/L	5.0 μmol/L	
AuNPs/CuTCPP(Fe)	Glucose	0.16–8 mmol/L	3.9 μmol/L	[163]
	Malachite green	–	0.16 mmol/L	
FP/Ag/ZIF-8	Thiram	–	4×10^{-11} mol/L	[164]
	4-Aminothiophenol	–	3×10^{-12} mol/L	
ZIF-8@GOx-AgNPs@MBN	Glucose	0–10 mmol/L	0.1 mmol/L	[165]
UiO-66@Ag NPs	Di-(2-ethylhexyl)phthalate	10^{-11}–10^{-4} mol/L	3×10^{-12} mol/L	[166]
Ag NPs/MIL-101	Dopamine	1.054 pmol/L–210.8 nmol/L	0.32 pmol/L	[167]
h-Ag NPs@MOF-1	D/L-Cysteine	–	–	[168]
	D/L-Asparagine	–	–	
Ag@HKUST-1	Polycyclic aromatic hydrocarbon	0.5 nmol/L–0.5 mol/L	–	[169]
Ag/Co-MOF	Congo red	0.1–1000 μmol/L	0.013 μmol/L	[170]
	Chrysoidine	0.1–1000 μmol/L	0.017 μmol/L	
	Acid orange II	0.01–100 μmol/L	0.0067 μmol/L	
ZIF-8@AgNPs	Rhodamine 6G	–	10^{-14} mol/L	[171]
Au@Ag_5@ZIF-8	Carbendazim	1.0×10^{-9}–1×10^{-5} mol/L	0.2 μg/kg	[172]
Au@Ag@ZIF-8	EGFR	–	–	[173]
	CD44	–	–	
AuAg@ZIF-8	Hexachlorocyclohexane	–	1.5 ppb	[174]
Au@Ag@ZIF-8	Aldehydes	–	1 ppb	[175]

oped substrates showed significant prospect as dependable SERS substrates for food contamination monitoring. The malachite green residue detection limit in prawns was 0.132 nmol/L. Yang *et al.* were capable of selectively depositing ZIF-8 on anisotropic Au nanobipyramids and nanorods by using a simple wet-chemistry technique [161]. In the experimental method, ZIF-8 was preferentially coated on the ends and waist of the elongated Au nanocrystals, as well as around the whole surface. The findings demonstrated that NBP-based structures featuring end-deposited ZIF-8 had the greatest SERS signals, indicating that the deposited ZIF-8 molecules might concentrate around hot regions. Furthermore, due to the molecular sieving function of ZIF-8, the compounded s constructions showed a bias towards identifying tiny molecules. In addition, vapor molecules were identified utilizing Au nanobipyramids with end-deposited ZIF-8, showing that ZIF-8 might capture vapor molecules and compress them to hot areas to detect in a SERS strategy. It was proposed that ZIF-8 could be deposited on plasmonic hot areas to boost SERS performance.

It is worth mentioning that some AuNPs/MOFs composites show interesting peroxidase properties and SERS activity, so it has been confirmed that AuNPs/MOF composites were employed through cascade reaction to improve the performance of SERS measurement. Hu *et al.* created a peroxidase-like nanozyme by growing AuNPs *in situ* in MIL-101, a type of MOF with high porosity and thermal stability [162]. They subsequently showed that not only the AuNPs@MIL-101 functioned as peroxidase mimics for catalytical transformation of Raman caged reporters to activated reporters, but also enhanced the Raman signal of active reporters as an active substrate simultaneously. Remarkably, the AuNPs@MIL-101 were then embellished with glucose oxidase and lactate oxidase (LOx) to generate AuNPs@MIL-101@GOx and AuNPs@MIL-101@LOx synthetic nanozymes, respectively, allowing for effective enzymatic cascade reactions. The synthetic nanozymes were subsequently employed to resoundingly detect glucose and lactate in real animal brains *via* SERS connected with ischemic stroke *in vitro*. The linear range of glucose was set in 10–200 μmol/L with a detection limit of 4.2 mol/L, whereas the linear range of lactate was 10–200 μmol/L with a detection limit of 5.0 μmol/L. Hu *et al.* first synthesized 2D metalloporphyrin Cu-TCPP(Fe) nanosheets with water stability, then prepared hybrid Au NPs/Cu-TCPP(Fe) nanosheets by *in situ* growth [163]. Cu-TCPP(Fe) nanosheets had peroxidase-mimetic performance while AuNPs possessed glucose oxidase mimicking property, which encouraged cascade catalysis reactions to transform glucose into H_2O_2 in the presence of O_2, and then H_2O_2 oxidized the leucomalachite green without Raman activity into the malachite green possessing Raman activity by employing AuNP. Synchronously, it made significant contributions to the SERS measurement of glucose with sensitivity and selectivity in the presence of AuNPs. Lastly, the SERS intensity of Raman active malachite green was measured in order to accomplish quantitative glucose detection with a LOD of 0.16 mmol/L.

2.4.2. Ag/MOFs

Except the Au NPs mentioned above, Ag NPs also exhibit good SERS activity and can be assembled with MOFs to synthesize SERS sensors based on Ag/MOFs composites [164–171]. Xu *et al.* created the FP/Ag/ZIF-8 SERS substrate, which was constituted of filter paper (FP), AgNPs, and ZIF-8 film layered in a hierarchi-

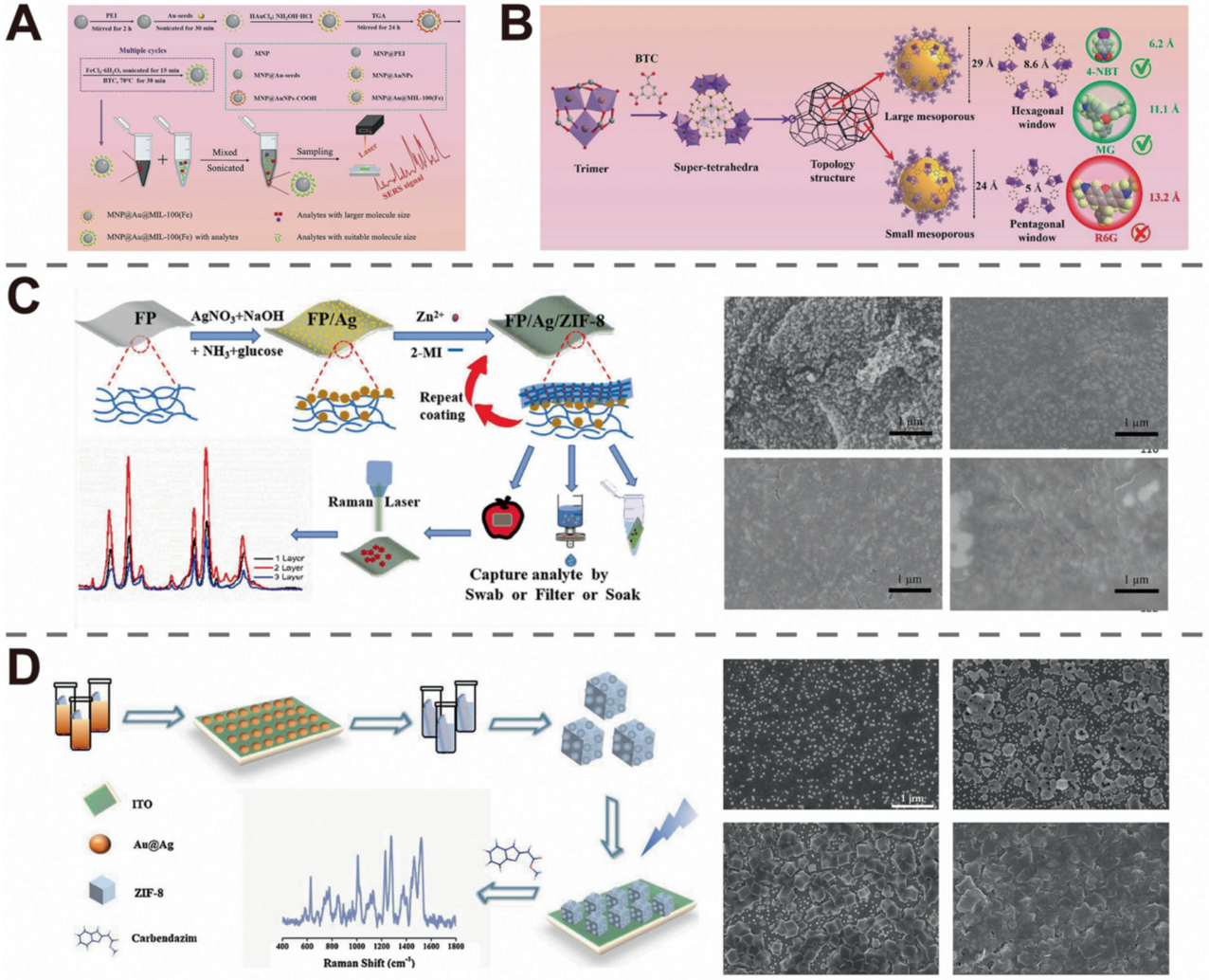

Fig. 8. (A) Schematic illustration of fabrication of MNP@Au@MIL-100(Fe) SERS substrate for selective SERS sensing. (B) Comparison between mesoporous window size of MIL-100(Fe) and hydrodynamic diameter of three different analyte molecules. (A,B) Reproduced with permission [160]. Copyright 2022, Wiley. (C) Schematic illustration of the formation of FP/Ag/ZIF-8 and its SERS detection procedure. SEM images of FP/Ag, FP/Ag/ZIF-8(1), FP/Ag/ZIF-8(2) and FP/Ag/ZIF-8(3). Reproduced with permission [164]. Copyright 2022, Elsevier. (D) Schematic illustration of preparation of ITO-Au@Ag5@ZIF-8 (1.5 h) chip and schematic diagram for detection of carbendazim in Seawater. SEM images of ITO-Au@Ag_5@ZIF-8 chip with different times of deposition are shown. Reproduced with permission [172]. Copyright 2021, Elsevier.

cal construction to effectively capture and detect pesticide thiram in diverse samples with sensitivity (Fig. 8C) [164]. To investigate the functions of their constituents in analyte adsorption and Raman signal amplification, they used the pesticide intermediate 4-aminothiophenol (4-ATP) as a probe. The SERS response was optimized on ZIF-8 thick film (125 nm) with satisfactory repeatability, great stability, and size-selective response to detect thiram, and the substrates had a distinct layered structure with outstanding adsorption capacity. Due to the synergistic interaction of the ingredients, the detection limit of 4-ATP was as low as 10^{-11} mol/L, which was three orders of magnitude lower than that of FP-Ag substrate. More crucially, because of its flexibility and porous structure, the FP-Ag/ZIF-8 could be used as an effective analyte capture approach by soaking, filtering, or swabbing to detect the pesticide thiram in different water or solution samples. Furthermore, certain AgNPs/MOF composites exhibited oxidase properties. It might take on the features of a cascade process by recombinating with other oxidases, so as to boost SERS activity. A bioinspired and biodegradable nanoreactor named as ZIF-8@GOx-AgNPs@MBN was created by Sun *et al.* for tumor chemo-starvation synergistic treatment and concurrent self-sense of cellular glucose levels [165]. The SERS nanoprobes (AgNPs@MBN) were electrostatically assembled on the GOx-encapsulated ZIF-8 nanoparticle (ZIF-8@GOx) to create the nanoreactor. Under the mild acidic microenvironment of tumor, after cancer cells had internalized the nanoreactors, the nanoreactors would crumble and liberate GOx, beginning a catalytic cascade that consumed glucose, corroded AgNPs@MBN, produced toxic H_2O_2, Ag^+ and Zn^{2+} ions, all of which acted collectively to suppress tumor development. As SERS nanoprobes, AgNPs@MBN could read the glucose levels in tumors noninvasively, providing instant feedback on treatment success. As a glucose biological detector, linearity response of the resultant SERS sensors ranged from 0 to 10 mmol/L with a LOD of 0.1 mmol/L.

2.4.3. AuAg/MOFs

In SERS sensors based on MNPs/MOFs, the combination of AuNPs and AgNPs has also been used as bimetallic NPs with SERS activity [172–175]. Zhai *et al.* successfully prepared Au@Ag modified ZIF-8 and then immobilized the composites on ITO glass to prevent superabundant nanoparticles agglomerating (Fig. 8D) [172]. The best SERS substrate was found to be the ITO-Au@Ag_5@ZIF-8 (1.5 h) chip, performing outstanding stability and Raman scattering enhancement. With the collective advantages of ITO-Au@Ag_5@ZIF-8 (1.5 h), as well as the adsorption capacity and aggregation capacity

Table 5
CL/ECL sensors based on MNPs/MOFs composites.

Nanomaterial	Analyte	Linear response range	Detection limit	Ref.
CuMOF/Co_3O_4	H_2O_2	1–250 nmol/L	0.244 nmol/L	[178]
Fe_3O_4/MIL-101(Fe)	H_2O_2	5–150 nmol/L	3.7 nmol/L	[179]
CuNCs@CuMOF	Tramadol	0.0030–2.5 μmol/L	0.80 nmol/L	[180]
Au@HKUST-1	Adeosine	4×10^{-13}–1.5×10^{-10} mol/L	1.04×10^{-13} mol/L	[181]
MOF@AuNP	Alpha-fetoprotein	0.64–10,000 pg/mL	0.36 pg/mL	[182]
Au&Pt@UiO-66	Protein kinase A	0.015–25 U/mL	0.009 U/mL	[183]
GSH-Au NCs@ZIF-8	Rutin	0.05–100 μmol/L	10 nmol/L	[186]
Co-MOFs/ABEI-Au	Amyloid-β protein	10 fg/mL–100 ng/mL	3 fg/mL	[187]
Pd-ZIF-67	Cytokerain 19 fragment 21-1	0.01–100 ng/mL	2.6 pg/mL	[188]
Luminol-Ag NPs@ZIF-67	Carbohydrate antigen 19-9	0.0001–10 U/mL	31 μU/mL	[189]
	Carbohydrate antigen 24-2	0.0005–10 U/mL	0.16 mU/mL	
Au@NiFeMOFs	Amyloid-β	100 fg/mL–50 ng/mL	13.8 fg/mL	[190]
AgNPs@Ru-MOF	Anatoxin-a	0.001–1 mg/mL	0.34 μg/mL	[191]

of target molecules, carbendazim could be identified in seawater by SERS technique. In practice, the ITO-Au@Ag_5@ZIF-8 (1.5 h)-chip-based Raman approach was able to detect carbendazim in seawater quickly and the broad linearity ranging from 1.0 nmol/L to 10 μmol/L. LOD in a saltwater sample could be as low as 0.2 μg/kg. Marchi *et al.* reported unique SERS tags with increased sensing performance by combining ZIF-8 with plasmonic nanoparticles synergistically, and reasonably engineered protein adaptors and antibodies [173]. The SERS tags were constructed out of Au@Ag core-shell nanorods encased in a multifunctional ZIF-8 framework with Raman reporters encoding. When the plasmonic core was to promote the Raman enhancement, the ZIF-8 captured the molecules of Raman activity, and more significantly, the activity targeting of SERS labeled surfaces was promoted *via* the modularized assembly of traditional antibodies and reorganizational antibodies mediated by the specific mutual effect between Zn^{2+} and polyhistidine-labeled protein G and SpyCatcher. The ability of Au@Ag@ZIF-8 nanotags to detect SERS on epidermal growth factor receptor (EGFR) and cluster of differentiation (CD44) cell surface receptors *in vitro* highlighted the optical prospects of nanoprobes for images and various biological detection.

In other words, porous MOFs not only increase MNPs uniformity and dispersion to prevent aggregation, but also enrich the target, enabling it easier to approach the surface of MNPs and thereby enhancing the SERS signal in surface-enhanced Raman scattering detection.

2.5. Chemiluminescence/electrochemiluminescence sensors

Chemiluminescence (CL) is defined as the emission of electromagnetic radiation caused by a chemical reaction. It forms an intermediate product in an electronically excited state and emits light as it relaxes to the ground state [176,177], which can be concisely defined as the chemical reaction of luminescence, while electrochemiluminescence (ECL) is an electrogenerated chemiluminescence phenomenon which has been intensively explored in past decades. In accordance with previous findings, MNPs/MOFs composites can be used to manufacture CL/ECL sensors, and improves the intensity and improving efficiency of CL/ECL on account of its excellent catalytic performance (Table 5).

2.5.1. MNPs/MOFs with catalytic activity in CL sensors

When it comes to the development of CL sensor, MNPs/MOFs composites have a promising application prospect because of its catalytic ability of CL reaction [178–183]. An effective CL system was presented by Amirzehni *et al.* to determine cholesterol and glucose on the basis of the considerable mimetic behavior of the CuMOF coated with cobalt oxide NPs (Co_3O_4@CuMOF) (Fig. 9A) [178]. The catalytic performance of nanocomposites was demonstrated by its ability to intensify the CL emission of the rhodamine B-H_2O_2 reaction. Additionally, while both virgin Co_3O_4 NPs and CuMOF boosted the CL signal of the rhodamine B-H_2O_2 system, their concurrent presence of the Co_3O_4@CuMOF nanocomposites enhanced the CL emission more effectively. The demonstrated synergetic catalytic activity was due to the presence of Cu and Co in the Co_3O_4@CuMOF structures, along with the high porosity and large surface areas of the produced composites. A linear relationship between CL intensity and H_2O_2 concentration was established throughout a large range of 1–250 nmol/L, with a detection limit of 0.244 nmol/L. They confirmed the exceptional sensitivity and selectivity of probe experimentally, which they attributed to the presence of Co_3O_4@CuMOF with great performance and the associated enzymes. Lin *et al.* constructed a CL biosensor for adenosine detection using a target-responsive DNA hydrogel with high loading capacity and biocompatibility [181]. To enrich adenosine and the controlled liberation of catalyst, the aforesaid DNA hydrogel was created. To regulate amplification of the chemiluminescence signal, Au@HKUST-1 with catalytic properties produced and encased in a DNA hydrogel. Only when adenosine along with hemin was present at the same time did the DNA hydrogel disintegrate. To synthesize Au@HKUST-1, Au NPs were coated into cavities of HKUST-1, a Cu-based MOF featuring peroxidase-mimetic performance. It was worth mentioning that the Au@HKUST-1 exhibited a greater peroxidase-mimetic performance than HKUST-1. After that, the DNA hydrogel was used to encapsulate Au@HKUST-1. Hemin bonded to the H-Apt to create the G-quadruplex/hemin when just hemin was present, and the DNA hydrogel maintained in the gel state. As a result, the G-quadruplex/hemin was produced, which allowed for the removal of superfluous heme and the avoidance of background signal disturbance. After that, adenosine was introduced, and the DNA hydrogel was fully dissolved due to the preferred mutual effects between adenosine and adenosine aptamer. G-quadruplex/hemin and Au@HKUST-1 were then liberated at the same time, overcoming the CL method's intrinsic sensitivity flaw by amplifying the dual signals of the chemiluminescence biosensor and creating signals at readout. The suggested CL biosensor was effectively employed for adenosine detection in urine, with the CL intensity proportionally related to adenosine concentration ranging from 0.4 pmol/L to 0.15 nmol/L and a LOD of 0.104 pmol/L was reached.

2.5.2. MOFs play a protective role in ECL sensors

Electrochemiluminescence is an energy-relaxation mechanism that results in excited-state photoemission when initiated by an intense electron-shift reaction [184,185]. To boost ECL efficiency, MNPs/MOFs composites can be employed to catalyze in ECL sensors. According to recent research, their composites can operate as efficient electrocatalysts in ECL sensing when paired with the catalytic activity of MNPs and the protective effect of MOFs. For example, Nie *et al.* built an Au NCs@MOF using a coordination-

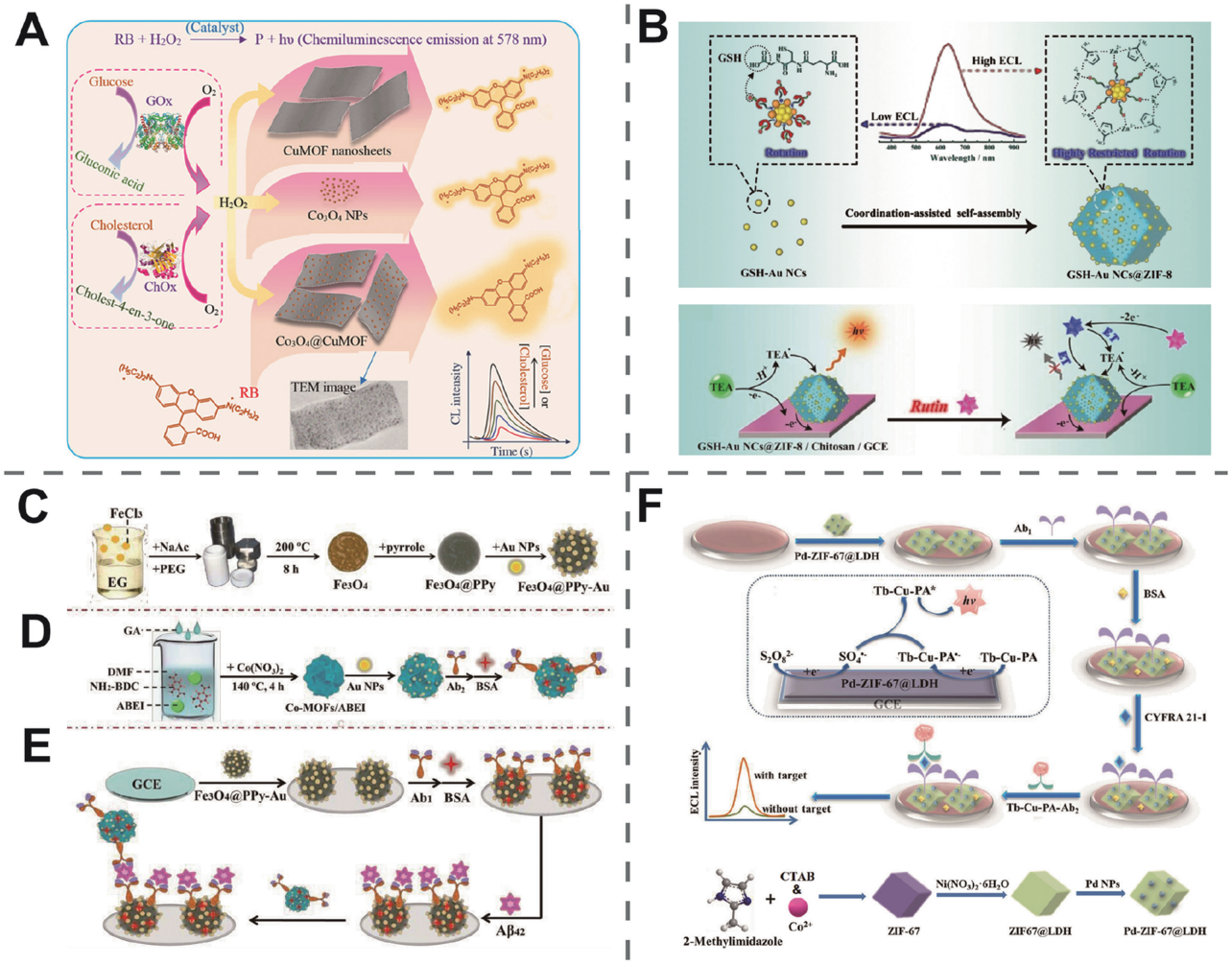

Fig. 9. (A) Schematic illustration of application of CuMOF nanosheets, Co_3O_4 NPs and mimic Co_3O_4@CuMOF for the determination of glucose and cholesterol using the CL detection system. TEM image of Co_3O_4@CuMOF is shown. Reproduced with permission [178]. Copyright 2021, Elsevier. (B) Schematic illustration of the preparation of GSH-Au NCs@ZIF-8 *via* coordination-assisted self-assembly strategy along with the ECL-enhanced mechanism and ECL turn-off strategy for the detection of rutin with GSH-Au NCs@ZIF-8/TEA system. Reproduced with permission [186]. Copyright 2021, American Chemical Society. (C) Schematic illustration for the preparation process of Fe_3O_4@PPy-Au. (D) Schematic illustration for the preparation process of Co-MOFs/ABEI-Au. (E) Schematic illustration for the fabrication process of the $A\beta_{42}$ immunosensor. (C–E): Reproduced with permission [187]. Copyright 2019, Elsevier. (F) Schematic illustration of construction diagram of immunosensor and ECL detection of CYFRA21-1. Reproduced with permission [188]. Copyright 2022, Elsevier.

assisted self-assembly strategy with Au NCs as one of the constructing units, which not only restricted the vibration and rotation of the NCs to achieve nonradiative transition constraint but also reduced the self-quenching efficiency due to the dispersion of Au NCs, thus considerably improving ECL efficiency (Fig. 9B) [186]. To demonstrate the concept, GSH-Au NCs@ZIF-8 was created by the traditional coordination interactions of Zn^{2+} with the carboxyl group in the GSH ligands together with the N atom of 2-methylimidazole linkers, whose ECL efficiency was 10-fold higher than that of merely aggregated Au NCs, based on the typical GSH protected Au NCs. They developed a signal-off sensing platform with a LOD as low as 10 nmol/L, which was characterized by excellent sensitivity, rapid response, convenience, and ease of use, employing rutin as an analyte.

2.5.3. Both MNPs and MOFs play a catalytic role

Similar to MNPs, some MOFs perform catalytic activity in ECL sensing applications as well, and these MNPs/MOFs composites are extensively used [187–189]. Wang *et al.* suggested a ternary electrochemiluminescence system that used *N*-(aminobutyl)-*N*-(ethylisoluminol) (ABEI) functionalized cobalt-based MOFs as the luminophore and had outstanding peroxidase-like activity (Fig. 9E) [187]. ABEI was used as a reduction agent and organic ligand in the production of flower-like Co-MOFs /ABEI (Fig. 9D). The prepared Co-MOFs/ABEI not only served as ideal carriers for ABEI gathering, but also as co-reaction boosters to catalyze H_2O_2 decomposition. In addition, electrostatic attraction was used to modify Au nanoparticles on Co-MOFs/ABEI, providing it with superior biocompatibility and catalytic properties, and allowing it to interact with detecting antibodies and create more excited state ABEI*. Furthermore, Fe_3O_4@polypyrrole functionalized gold nanoparticles had large specific surface areas and were easy to prepare (Fig. 9C), and the captured antibody was immobilized with the target analyte. The major hallmark of Alzheimer's disease, amyloid beta protein ($A\beta_{42}$), was investigated. The LOD is 3 fg/mL, with the linear response ranging from 10 fg/mL to 100 ng/mL. The developed ECL immunosensor could recognize $A\beta_{42}$, so it opened up a new avenue for $A\beta_{42}$ clinical investigation. Zhou *et al.* proposed employing copper doped Tb MOF as an ECL emitter to develop a sensitive ECL immunosensing technique for the detection of cytokeratin 19 fragment 21-1 (CYFRA21-1) (Fig. 9F) [188]. With $K_2S_2O_8$ as a co-reactant, the Tb-Cu-PA MOF was synthesized by utilizing Tb^{3+} and Cu^{2+} ions as metal linkers while m-phthalic acid was used as bridge ligands, and showed significant ECL emissions. Cu boosted

the size, constructure, and ECL emission of MOF, labeled the signal antibody successfully and improved increasing detection sensitivity. To fabricate the ECL sensor, Pd nanoparticles were grown on the ZIF-67@LDH nanoboxes. The Pd-ZIF-67@LDH modified electrode could be used to conveniently prepare the immunosensor and load the antibody. The reduction of $S_2O_8^{2-}$ by Pd-ZIF-67@LDH had a high conductivity and electrocatalytic performance, allowing ECL signals to be amplified. Tb-Cu-PA MOF tagged antibody was placed on the obtained sensor after the sandwich-typed immunoreactions to detect the sensitivity of ECL signals of the target protein. The ECL immunosensing approach was linear in the range of 0.01–100 ng/mL, with a LOD of 2.6 pg/mL, applying cytokeratin 19 fragment 21-1 as the target analyte.

2.5.4. Dual quenching ECL sensors

In accordance with recent research, MNPs/MOFs composites may be utilized to synthesize dual quenching ECL immunosensors, which has a broad application prospect. A dual-quenching ECL immunosensor was presented by Zhao *et al.* to ultrasensitively detect amyloid-β (Aβ) on the basis of $Ru(bpy)_3^{2+}$ encased in Zn-oxalate MOF as the luminophor and Au@NiFe MOFs as the double quenchers [190]. Because the ECL efficiency of Au NPs and NiFe-based MOFs as ECL acceptors in resonance energy transfer (RET) process might be quenched, the as-obtained Au@NiFe MOFs with high porosity might reduce the ECL intensity of $Ru(bpy)_3^{2+}$/Zn-oxalate MOFs composites. Thus, the sensitivity of the immunosensor was greatly enhanced. Besides, the UV-visible absorption spectrum of Au@NiFe MOFs matched the ECL emission spectra of $Ru(bpy)_3^{2+}$/zin-oxalate MOFs, indicating that the molecule had a dual quenching effect. In addition, the proposed dual quenching ECL immunosensor demonstrated remarkable selectivity, durability, and repeatability, indicating a potential quenching approach for Aβ determination. A linearity detection range of 100 fg/mL–50 ng/mL was obtained when detecting Aβ to identify whether it was clinically useful, with a LOD of 13.8 fg/mL. Xia *et al.* proposed an ECL-RET approach to sensitively and reliably detect anatoxin-a (ATX-a), with dual-quenched extremely low background signals and a dual-stimuli response and correct signal production [191]. The created sensor not only aided in the creation of a double quenching ECL-RET system, but also in the development of an ECL biosensing platform with multi-stimulus response, which had wide applications in complex sample analysis. The combined ECL-RET probe enabled dual quenching of MOF encased in Ru-MOF, covered with AgNPs shell, and in compact contact with DNA-ferrocene. Between ATX-a and H_2O_2, the multistimulus response DNAzyme facilitated correct signal conversion. A complicated DNA sequence design revealed Ag^+ dependent DNAzyme sequences due to the aptamer's unique identification of ATX-a. Ag^+ generated *in situ* by H_2O_2, which started a catalytic cleavage event that released two ECL-RET energy acceptors, substantially flipping ECL signals and enabling ultra-sensitive detection. AgNPs played a vital role in the ECL-RET technique, acting as gate-keepers to prevent ECL probe leakage, as well as ECL energy acceptors and, most critically, as the redox substrates for the following DNAzyme catalytic signal switch. The supplied ECL-RET aptasensor to detect ATX-a performed well, with a linear relation between ECL signals and ATX-a concentrations ranging from 1 μg/mL to 1 mg/mL and a detection limit of 0.34 μg/mL.

To summarize, the synergistic interaction of MNP and MOF results in increased CL/ECL intensity and enhanced CL/ECL sensing efficiency in MNPs/MOFs composites.

3. Conclusions and outlook

Over the last decade, the number of sensors on the basis of MNPs/MOFs composites has increased sharply. Applications of MNPs/MOFs composites in different fields of sensing and their synergistic effects in improving the sensing exhibition are introduced. Then, according to the types of sensors based on MNPs/MOFs composites, they are divided into different sensors involving electrochemical sensing, fluorescent sensing, colorimetric sensing, SERS sensing and CL/ECL sensing, which are introduced emphatically. Particularly, the characteristics of MNPs and MOFs are reviewed, which have synergistic processes are commonly used to classify the mutual effects of MNPs and MOFs: (1) MNPs function as active centers while MOFs have a stabilizing effect on MNPs. (2) Easily aggregable MNPs are limited in MOFs to ensure signal certainty. (3) Owing to the high porosity of MOFs, it is possible to ensure the entry of suitable sized reactants, which then react with the MNPs as active centers. (4) Either MNPs or MOFs function as active sites for tandem catalysis.

As mentioned above, we have made great achievements in the past decades or so but the field of sensing is still underdeveloped and joint efforts should be further made in the future development of MNPs/MOFs in sensing. Several inadequate but expected issues on the basis of MNPs/MOFs are demonstrated as follows.

(1) According to current reports on MNPs/MOFs, though the encapsulation in or on the outer surface of MOFs can be reasonably regulated, MNPs are confined to unordered arrangements. Owing to the constitutional mutual effects between the MNPs, periodic arrays of MNPs can greatly improve their characteristics. Consequently, it would be satisfying to develop effective strategies to achieve superior spatial arrangement of MNPs, whose size, shape and distribution are well managed within MOFs, which will benefit sensing performance.
(2) Both precious metal nanoparticles and bimetallic nanoparticles consisting of precious metals and base metals, exhibit sensing performance with great promise through associating with MOFs. It is found that Au NPs and Ag NPs appear frequently in numerous reports. Nevertheless, it is quite realistic that there are concerns about rareness and expensiveness of noble metals. In MNPs/MOFs used for sensing, base metal NPs should be considered instead of noble metal NPs.
(3) Because of the dilemma of developing MOFs featuring uniform and adequately tiny sizes, the implementation of a stable and repeatable response for sensors on the basis of MNPs/MOFs composites is a challenge. The application of nano-MOF in MNPs/MOFs composites will significantly advance the sensing capabilities including stability, sensitivity and responsive time.
(4) Advances in MNPs/MOFs cannot be divorced from MOFs research. It is essential to build highly stable MOFs with scalar holes and customizable hole conditions since large aperture eliminates mass transfer constraints and pore wall circumstances permit to customize electronic characteristics of MNPs.
(5) Highly customizable pore circumstances in MOFs contribute to modulating sensing performance of encased MNPs and offer a wide range of applications in sensing, which is still immature in spite of numerous reports. Functional groups suspended from the connectives not only have the capability of adjusting the electronic states of MNPs in the absence of additional stimuli, but also provide a limited reaction space to optimize the sensing performance.
(6) Additionally, MNPs/MOFs composites can be combined with other nanomaterials, such as MNPs/metal oxide/graphene oxide, and MOFs may be more formidable sensors. Since the sensing performance of MNPs depends upon the quality of the scaffold, introducing this special scaffold along with MNP/support mutual effects to MOFs will enhance the sensing exhibition of MNPs. At the same time, as this review has indicated, the versatility of MOFs can be combined with MNPs to greatly improve sensing performance.

In conclusion, the controllable introduction of MNPs in or on MOF is supposed to optimize the synergistic mechanism of MNPs/MOFs composites in the applications of sensing. Despite these obstacles, we reasonably believe that MNPs/MOFs composites enjoy a promising prospect in various sensing fields.

Declaration of competing interest

The authors declare that they have no known competing financial interests or personal relationships that could have appeared to influence the work reported in this paper.

Acknowledgments

This work was supported by the National Natural Science Foundation of China (No. NSFC-U1904215), Natural Science Foundation of Jiangsu Province (No. BK20200044), Program for Young Changjiang Scholars of the Ministry of Education, China (No. Q2018270). We also acknowledge the Priority Academic Program Development of Jiangsu Higher Education Institutions and the technical support we received at the Testing Center of Yangzhou University.

References

[1] M. Brust, C.J. Kiely, Colloid. Surf. A 202 (2002) 175–186.
[2] S. Mourdikoudis, R.M. Pallares, N.T.K. Thanh, Nanoscale 10 (2018) 12871–12934.
[3] K. Saha, S.S. Agasti, C. Kim, X. Li, V.M. Rotello, Chem. Rev. 112 (2012) 2739–2779.
[4] N. Li, X. Su, Y. Lu, Analyst 140 (2015) 2916–2943.
[5] S.R. Emory, W.E. Haskins, S. Nie, J. Am. Chem. Soc. 120 (1998) 8009–8010.
[6] F. Saleem, X. Cui, Z. Zhang, et al., Small 15 (2019) 1903253.
[7] Y.U. Staechelin, D. Hoeing, F. Schulz, H. Lange, ACS Photonics 8 (2021) 752–757.
[8] C. Voisin, D. Christofilos, N. Del Fatti, et al., Phys. Rev. Lett. 85 (2000) 2200–2203.
[9] R.M. Pallares, P. Choo, L.E. Cole, et al., Bioconjug. Chem. 30 (2019) 2032–2037.
[10] X. Zhou, H. Pu, D.W. Sun, Crit. Rev. Food Sci. Nutr. 61 (2021) 2277–2296.
[11] I. Chakraborty, W.J. Parak, Adv. Mater. Interfaces 6 (2019) 1970037.
[12] I. Chakraborty, W.J. Parak, Adv. Mater. Interfaces 6 (2019) 1801407.
[13] N. Gogurla, A.K. Sinha, D. Naskar, S.C. Kundu, S.K. Ray, Nanoscale 8 (2016) 7695–7703.
[14] R.M. Pallares, N.T.K. Thanh, X. Su, Nanoscale 11 (2019) 22152–22171.
[15] L. Wang, M. Hasanzadeh Kafshgari, M. Meunier, Adv. Funct. Mater. 30 (2020) 2005400.
[16] I. Fratoddi, R. Matassa, L. Fontana, et al., J. Phys. Chem. C 121 (2017) 18110–18119.
[17] C. Zhu, G. Yang, H. Li, D. Du, Y. Lin, Anal. Chem. 87 (2015) 230–249.
[18] P.A. Rasheed, N. Sandhyarani, Microchim. Acta 184 (2017) 981–1000.
[19] A. Abbas, H.M.A. Amin, Microchem. J. 175 (2022) 107166.
[20] P.K. Jain, X. Huang, I.H. El-Sayed, M.A. El-Sayed, Acc. Chem. Res. 41 (2008) 1578–1586.
[21] V. Myroshnychenko, J. Rodríguez-Fernández, I. Pastoriza-Santos, et al., Chem. Soc. Rev. 37 (2008) 1792.
[22] J.A. Creighton, D.G. Eadon, J. Chem. Soc. Faraday Trans. 87 (1991) 3881–3891.
[23] P. Kanninen, C. Johans, J. Merta, K. Kontturi, J. Colloid. Interface Sci. 318 (2008) 88–95.
[24] Q.L. Zhu, Q. Xu, Chem 1 (2016) 220–245.
[25] Q. Zhang, I. Lee, J.B. Joo, F. Zaera, Y. Yin, Acc. Chem. Res. 46 (2013) 1816–1824.
[26] N. Wang, Q. Sun, J. Yu, Adv. Mater. 31 (2019) 1803966.
[27] L. Chen, R. Luque, Y. Li, Chem. Soc. Rev. 46 (2017) 4614–4630.
[28] Q. Wang, D. Astruc, Chem. Rev. 120 (2020) 1438–1511.
[29] C. Gao, F. Lyu, Y. Yin, Chem. Rev. 121 (2021) 834–881.
[30] G. Férey, C. Mellot-Draznieks, C. Serre, et al., Science 309 (2005) 2040–2042.
[31] H. Deng, S. Grunder, K.E. Cordova, et al., Science 336 (2012) 1018–1023.
[32] R.S.K. Madsen, A. Qiao, J. Sen, et al., Science 367 (2020) 1473–1476.
[33] S. Wang, C.M. McGuirk, A. D'Aquino, J.A. Mason, C.A. Mirkin, Adv. Mater. 30 (2018) 1800202.
[34] R. Zhao, Z. Liang, R. Zou, Q. Xu, Joule 2 (2018) 2235–2259.
[35] C. Hou, Q. Xu, Adv. Energy Mater. 9 (2019) 1801307.
[36] S. Abednatanzi, P.G. Derakhshandeh, H. Depauw, et al., Chem. Soc. Rev. 48 (2019) 2535–2565.
[37] K. Jayaramulu, F. Geyer, A. Schneemann, et al., Adv. Mater. 31 (2019) 1970230.
[38] A.E. Thorarinsdottir, T.D. Harris, Chem. Rev. 120 (2020) 8716–8789.
[39] K. Shen, L. Zhang, X. Chen, et al., Science 359 (2018) 206–210.
[40] S. Dutta, J. Kim, P. Hsieh, et al., Small Methods 3 (2019) 1900213.
[41] S.L. Anderson, P.G. Boyd, A. Gładysiak, et al., Nat. Commun. 10 (2019) 1612.
[42] H. Cai, Y.L. Huang, D. Li, Coord. Chem. Rev. 378 (2019) 207–221.
[43] Y. Liu, Z. Liu, D. Huang, et al., Coord. Chem. Rev. 388 (2019) 63–78.
[44] Q. Yang, Q. Xu, H. Jiang, Chem. Soc. Rev. 46 (2017) 4774–4808.
[45] S. Liu, C. Lai, X. Liu, et al., Coord. Chem. Rev. 424 (2020) 213520.
[46] Y. Xue, S. Zheng, H. Xue, H. Pang, J. Mater. Chem. A 7 (2019) 7301–7327.
[47] G. Li, S. Zhao, Y. Zhang, Z. Tang, Adv. Mater. 30 (2018) 1800702.
[48] B. Li, J. Ma, P. Cheng, Small 15 (2019) 1804849.
[49] W. Cui, T. Hu, Small 17 (2021) 2003971.
[50] X. Kang, M. Zhu, Chem. Soc. Rev. 48 (2019) 2422–2457.
[51] H. Yu, B. Rao, W. Jiang, S. Yang, M. Zhu, Coord. Chem. Rev. 378 (2019) 595–617.
[52] Q. Tang, G. Hu, V. Fung, D. Jiang, Acc. Chem. Res. 51 (2018) 2793–2802.
[53] L. Shang, J. Xu, G.U. Nienhaus, Nano Today 28 (2019) 100767.
[54] Z. Guo, C. Xiao, R.V. Maligal-Ganesh, et al., ACS Catal. 4 (2014) 1340–1348.
[55] Y. Yang, F. Wang, Q. Yang, et al., ACS Appl. Mater. Interfaces 6 (2014) 18163–18171.
[56] J. Zhou, P. Wang, C. Wang, et al., ACS Nano 9 (2015) 6951–6960.
[57] Y. Huang, M. Zhao, S. Han, et al., Adv. Mater. 29 (2017) 1700102.
[58] X. Wang, Y. Wang, Y. Ying, Trac Trend Anal. Chem. 143 (2021) 116395.
[59] L. Dong, L. Yin, G. Tian, et al., Sens. Actuator. B: Chem. 308 (2020) 127687.
[60] H. Zhao, X. Du, H. Dong, et al., Biosens. Bioelectron. 175 (2021) 112883.
[61] E. Ma, P. Wang, Q. Yang, et al., ACS Biomater. Sci. Eng. 6 (2020) 1418–1427.
[62] Y. Zhang, Z. Zhang, S. Rong, et al., Microchim. Acta 187 (2020) 264.
[63] K. Zhang, K. Dai, R. Bai, et al., Chin. Chem. Lett. 30 (2019) 664–667.
[64] C. Zhang, J. He, Y. Zhang, et al., Biosens. Bioelectron. 102 (2018) 94–100.
[65] J. Jiang, Q. Cai, M. Deng, Front. Chem. 9 (2022) 812983.
[66] Y. Sun, X. Jiang, H. Jin, R. Gui, Anal. Chim. Acta 1083 (2019) 101–109.
[67] H. Lei, H. Zhu, S. Sun, et al., Electrochim. Acta 365 (2021) 137375.
[68] V.K. Bajpai, Y. Haldorai, I. Khan, et al., Microchim. Acta 188 (2021) 365.
[69] H. Chen, T. Yang, F. Liu, W. Li, Sens. Actuator. B: Chem. 286 (2019) 401–407.
[70] A. Paul, G. Vyas, P. Paul, D.N. Srivastava, ACS Appl. Nano Mater. 1 (2018) 3600–3607.
[71] L. Wang, T. Meng, Y. Fan, et al., J. Colloid. Interface Sci. 524 (2018) 1–7.
[72] X. Meng, H. Gu, H. Yi, et al., Anal. Chim. Acta 1125 (2020) 1–7.
[73] M. Deng, X. Bo, L. Guo, J. Electroanal. Chem. 815 (2018) 198–209.
[74] L. Ma, Y. He, Y. Wang, et al., Electrochim. Acta 318 (2019) 525–533.
[75] J. Chen, C. Yu, Y. Zhao, et al., Biosens. Bioelectron. 91 (2017) 892–899.
[76] L. Xu, J. Li, J. Zhang, et al., Analyst 145 (2020) 3245–3256.
[77] P. Ling, J. Lei, L. Jia, H. Ju, Chem. Commun. 52 (2016) 1226–1229.
[78] L. Zhang, S. Li, J. Xin, et al., Microchim. Acta 186 (2019) 9.
[79] X. Zhou, S. Guo, J. Gao, et al., Biosens. Bioelectron. 98 (2017) 83–90.
[80] A. Samadi-Maybodi, S. Ghasemi, H. Ghaffari-Rad, Sens. Actuator. B: Chem. 220 (2015) 627–633.
[81] S. Dong, D. Zhang, G. Suo, W. Wei, T. Huang, Anal. Chim. Acta 934 (2016) 203–211.
[82] Z. Peng, Z. Jiang, X. Huang, Y. Li, RSC Adv. 6 (2016) 13742–13748.
[83] P. Arul, S.A. John, Electrochim. Acta 235 (2017) 680–689.
[84] Y. Zhao, J. Chen, H. Zhong, et al., Microchim. Acta 187 (2020) 649.
[85] X. Li, J. Miao, Y. Li, et al., ACS Appl. Nano Mater. 2 (2019) 8043–8050.
[86] D. Kwon, J. Kim, J. Appl. Electrochem. 51 (2021) 1207–1216.
[87] Y. Wang, P. Dong, J. Huang, et al., Anal. Chim. Acta 1184 (2021) 339036.
[88] A.T. Ezhil Vilian, B. Dinesh, R. Muruganantham, et al., Microchim. Acta 184 (2017) 4793–4801.
[89] L. Wang, T. Meng, L. Liang, et al., Sens. Actuator. B: Chem. 278 (2019) 133–139.
[90] T. Meng, N. Shang, A. Nsabimana, et al., Anal. Chim. Acta 1138 (2020) 59–68.
[91] Q. Zhu, S. Hu, L. Zhang, et al., Sens. Actuator. B: Chem. 313 (2020) 128031.
[92] L. Shi, X. Zhu, T. Liu, H. Zhao, M. Lan, Sens. Actuator. B: Chem. 227 (2016) 583–590.
[93] Y. Shu, Y. Yan, J. Chen, et al., ACS Appl. Mater. Interfaces 9 (2017) 22342–22349.
[94] X. Yang, J. Lv, Z. Yang, R. Yuan, Y. Chai, Anal. Chem. 89 (2017) 11636–11640.
[95] Y. Yu, C. Yu, Y. Niu, et al., Biosens. Bioelectron. 101 (2018) 297–303.
[96] Y. Wang, G. Zhao, G. Zhang, et al., Sens. Actuator. B: Chem. 319 (2020) 128313.
[97] J. Yang, L. Yang, H. Ye, F. Zhao, B. Zeng, Electrochim. Acta 219 (2016) 647–654.
[98] Y. Wang, Y. Wang, F. Wang, et al., J. Colloid. Interface Sci. 606 (2022) 510–517.
[99] S.A. Hira, M. Nallal, K.H. Park, Sens. Actuator. B: Chem. 298 (2019) 126861.
[100] J. Zhang, X. Xu, Y. Qiang, Sens. Actuator. B: Chem. 312 (2020) 127964.
[101] J. Ma, J. Zheng, Microchim. Acta 187 (2020) 389.
[102] S. Li, S. Yue, C. Yu, et al., Analyst 144 (2019) 649–655.
[103] H. Wang, W. Chen, Q. Chen, et al., J. Electroanal. Chem. 897 (2021) 115603.
[104] Z. Chen, Y. Qian, L. Zhang, Y. Tian, J. Electroanal. Chem. 905 (2022) 115985.
[105] W. Meng, Y. Wen, L. Dai, Z. He, L. Wang, Sens. Actuator. B: Chem. 260 (2018) 852–860.
[106] L. Dai, Y. Li, Y. Wang, et al., Biosens. Bioelectron. 132 (2019) 97–104.
[107] Y. Dong, C. Duan, Q. Sheng, J. Zheng, Analyst 144 (2019) 521–529.
[108] D. Sun, D. Yang, P. Wei, et al., ACS Appl. Mater. Interfaces 12 (2020) 41960–41968.
[109] Y. Yang, Z. Yang, J. Lv, R. Yuan, Y. Chai, Talanta 169 (2017) 44–49.
[110] D. Duan, H. Yang, Y. Ding, et al., Electrochim. Acta 261 (2018) 160–166.
[111] M. Wang, L. Yang, B. Hu, et al., Appl. Surf. Sci. 445 (2018) 123–132.
[112] J. Liu, Y. Shang, Q. Zhu, X. Zhang, J. Zheng, Microchim. Acta 186 (2019) 509.
[113] S. Chen, P. Zhao, L. Jiang, et al., Anal. Bioanal. Chem. 413 (2021) 613–624.
[114] X. Zhang, M. Zhu, Y. Jiang, et al., J. Hazard. Mater. 400 (2020) 123222.
[115] H. Dong, X. Hu, J. Zhao, et al., Sens. Actuator. B: Chem. 276 (2018) 150–157.
[116] T. Yan, L. Zhu, H. Ju, J. Lei, Anal. Chem. 90 (2018) 14493–14499.
[117] Y.C. Wang, Y.C. Chen, W.S. Chuang, ACS Appl. Nano Mater. 3 (2020) 9440–9448.

[118] Y. Wang, L. Wang, H. Chen, X. Hu, S. Ma, ACS Appl. Mater. Interfaces 8 (2016) 18173–18181.
[119] Q. Wang, X. Zhang, X. Chai, et al., ACS Appl. Nano Mater. 4 (2021) 6103–6110.
[120] L. Chen, T. Wang, Y. Xue, et al., Adv. Mater. Interfaces 5 (2018) 1801168.
[121] J. Yang, H. Ye, F. Zhao, B. Zeng, ACS Appl. Mater. Interfaces 8 (2016) 20407–20414.
[122] C. Li, R. Wu, J. Zou, et al., Biosens. Bioelectron. 116 (2018) 81–88.
[123] Y. Lu, W. Chen, Chem. Soc. Rev. 41 (2012) 3594.
[124] J. Sun, Y. Jin, J. Mater. Chem. C 2 (2014) 8000–8011.
[125] Y. Tao, M. Li, J. Ren, X. Qu, Chem. Soc. Rev. 44 (2015) 8636–8663.
[126] R. Jin, Nanoscale 2 (2010) 343–362.
[127] Q. Tan, R. Zhang, G. Zhang, et al., Anal. Bioanal. Chem. 412 (2020) 1317–1324.
[128] X. Cao, S. Cheng, Y. You, S. Zhang, Y. Xian, Anal. Chim. Acta 1092 (2019) 108–116.
[129] M. Xia, Y. Sui, Y. Guo, Y. Zhang, Analyst 146 (2021) 904–910.
[130] R. Jalili, M. Dastborhan, S. Chenaghlou, A. Khataee, J. Photochem. Photobiol. A Chem. 391 (2020) 112370.
[131] B. Han, X. Hu, M. Yu, et al., RSC Adv. 8 (2018) 22748–22754.
[132] X.J. Wu, F. Kong, C.Q. Zhao, S.N. Ding, Analyst 144 (2019) 2523–2530.
[133] C. Fan, X. Lv, F. Liu, et al., ACS Sens. 3 (2018) 441–450.
[134] N. Bagheri, A. Khataee, B. Habibi, J. Hassanzadeh, Talanta 179 (2018) 710–718.
[135] L. Liu, Y. Hao, Z. Li, et al., Chem. Pap. 74 (2020) 1839–1847.
[136] L. Zhang, C. Fan, M. Liu, et al., Sens. Actuator. B: Chem. 266 (2018) 543–552.
[137] X. Wang, H. Wang, L. Guo, et al., Analyst 145 (2020) 1362–1367.
[138] N. Bagheri, A. Khataee, J. Hassanzadeh, B. Habibi, J. Hazard. Mater. 360 (2018) 233–242.
[139] H. Wang, J. Zhao, C. Liu, Y. Tong, W. He, ACS Omega 6 (2021) 4807–4815.
[140] H. Li, H. Liu, J. Zhang, et al., ACS Appl. Mater. Interfaces 9 (2017) 40716–40725.
[141] T. Cheng, X. Li, P. Huang, et al., Microchim. Acta 186 (2019) 94.
[142] Q. Luan, X. Xiong, N. Gan, et al., Talanta 187 (2018) 27–34.
[143] J. Li, J. Zhao, S. Li, et al., Nano Res. 14 (2021) 4689–4695.
[144] Y. Wu, Y. Ma, G. Xu, et al., Sens. Actuator. B: Chem. 249 (2017) 195–202.
[145] Z. Hu, Y. Yin, Q. Liu, X. Zheng, Analyst 144 (2019) 2716–2724.
[146] J. Li, K. Xu, Y. Chen, Chemosensors 9 (2021) 140.
[147] Y. Zhang, J. Song, Q. Pan, et al., J. Mater. Chem. B 8 (2020) 114–124.
[148] Y. Liu, L. Zhang, Q. Li, et al., Anal. Chim. Acta 1146 (2021) 24–32.
[149] H. Yang, Z. Sun, X. Qin, et al., Food Chem. 376 (2022) 131906.
[150] H. Chen, Q. Qiu, S. Sharif, et al., ACS Appl. Mater. Interfaces 10 (2018) 24108–24115.
[151] J. Chi, M. Guo, C. Zhang, et al., New J. Chem. 44 (2020) 13344–13349.
[152] J. Feng, H. Lu, Y. Yang, et al., Microchim. Acta 188 (2021) 280.
[153] G. Cai, K. Ge, X. Ouyang, Y. Hu, G. Li, J. Sep. Sci. 43 (2020) 2834–2841.
[154] S. Park, C. Bae, J. Lee, et al., ACS Appl. Nano Mater. 4 (2021) 14004–14013.
[155] H. Kim, B.T. Trinh, K.H. Kim, et al., Biosens. Bioelectron. 179 (2021) 113063.
[156] Q. Wang, Z. Shi, Z. Wang, et al., Anal. Chim. Acta 1129 (2020) 126–135.
[157] L. Wu, H. Pu, L. Huang, D.W. Sun, Food Chem. 328 (2020) 127105.
[158] J. Fu, H. Lai, Z. Zhang, G. Li, Anal. Chim. Acta 1161 (2021) 338464.
[159] Y. Hu, J. Liao, D. Wang, G. Li, Anal. Chem. 86 (2014) 3955–3963.
[160] H. Pu, H. Zhu, F. Xu, D. Sun, J. Raman Spectrosc. 53 (2022) 682–693.
[161] X. Yang, Y. Liu, S.H. Lam, et al., Nano Lett. 21 (2021) 8205–8212.
[162] Y. Hu, H. Cheng, X. Zhao, et al., ACS Nano 11 (2017) 5558–5566.
[163] S. Hu, Y. Jiang, Y. Wu, et al., ACS Appl. Mater. Interfaces 12 (2020) 55324–55330.
[164] F. Xu, W. Shang, M. Xuan, G. Ma, Z. Ben, Chemosphere 288 (2022) 132635.
[165] D. Sun, G. Qi, K. Ma, et al., iScience 23 (2020) 101274.
[166] H. Xu, J. Zhu, Y. Cheng, D. Cai, Sens. Actuator. B: Chem. 349 (2021) 130793.
[167] Z. Jiang, P. Gao, L. Yang, C. Huang, Y. Li, Anal. Chem. 87 (2015) 12177–12182.
[168] X. Kuang, S. Ye, X. Li, et al., Chem. Commun. 52 (2016) 5432–5435.
[169] D. Li, X. Cao, Q. Zhang, et al., J. Mater. Chem. A 7 (2019) 14108–14117.
[170] Q. Wang, Z. Xu, Y. Zhao, et al., Sens. Actuator. B: Chem. 329 (2021) 129080.
[171] X. Ren, M. Jin, X. Feng, X. Li, Y. Zhou, Appl. Surf. Sci. 537 (2021) 147853.
[172] Y. Zhai, T. Xuan, Y. Wu, et al., Sens. Actuator. B: Chem. 326 (2021) 128852.
[173] S.D. Marchi, L. Vázquez-Iglesias, G. Bodelón, et al., Chem. Mater. 32 (2020) 5739–5749.
[174] X. Zhou, G. Liu, H. Zhang, Y. Li, W. Cai, J. Hazard. Mater. 368 (2019) 429–435.
[175] K. Yang, S. Zong, Y. Zhang, et al., ACS Appl. Mater. Interfaces 12 (2020) 1395–1403.
[176] Y. Su, Y. Xie, X. Hou, Y. Lv, Appl. Spectrosc. Rev. 49 (2014) 201–232.
[177] S. Han, Z. Zhang, S. Li, L. Qi, G. Xu, Sci. China Chem. 59 (2016) 794–801.
[178] M. Amirzehni, H. Eskandari, B. Vahid, J. Hassanzadeh, Sens. Actuator. B: Chem. 348 (2021) 130690.
[179] X. Tang, Y. Zhang, Z. Jiang, et al., Talanta 179 (2018) 43–50.
[180] A. Yousefzadeh, J. Hassanzadeh, S.M.J. Mousavi, M. Yousefzadeh, Sens. Actuator. B: Chem. 286 (2019) 154–162.
[181] Y. Lin, X. Wang, Y. Sun, et al., Sens. Actuator. B: Chem. 289 (2019) 56–64.
[182] Y. Li, J. Yuan, S. Zhan, et al., Sens. Actuator. B: Chem. 341 (2021) 130030.
[183] Z. Yan, F. Wang, P. Deng, et al., Biosens. Bioelectron. 109 (2018) 132–138.
[184] F. Wang, J. Lin, T. Zhao, et al., J. Am. Chem. Soc. 138 (2016) 7718–7724.
[185] H. Peng, Z. Huang, H. Deng, et al., Angew. Chem. Int. Ed. 59 (2020) 9982–9985.
[186] Y. Nie, X. Tao, H. Zhang, Y. Chai, R. Yuan, Anal. Chem. 93 (2021) 3445–3451.
[187] C. Wang, N. Zhang, Y. Li, et al., Sens. Actuator. B: Chem. 291 (2019) 319–328.
[188] L. Zhou, L. Yang, C. Wang, et al., Talanta 238 (2022) 123047.
[189] G. Mo, X. He, D. Qin, et al., Biosens. Bioelectron. 178 (2021) 113024.
[190] G. Zhao, Y. Wang, X. Li, et al., Anal. Chem. 91 (2019) 1989–1996.
[191] M. Xia, F. Zhou, X. Feng, et al., Anal. Chem. 93 (2021) 11284–11290.